Computational Investigations on Carbon Dioxide Adsorption in Porous Framework Solids

A Thesis submitted in partial fulfillment

for the degree of

MASTER OF SCIENCE

as a part of the

Integrated Ph.D. programme

(Chemical Science)

by

Promit Ray

NEW CHEMISTRY UNIT
JAWAHARLAL NEHRU CENTRE FOR ADVANCED SCIENTIFIC RESEARCH
Bangalore – 560 064, India

APRIL 2015

DECLARATION

I hereby declare that the matter embodied in the thesis entitled "**Computational Investigations on Carbon Dioxide Adsorption in Porous Framework Solids**" is the result of investigations carried out by me at the New Chemistry Unit, Jawaharlal Nehru Centre for Advanced Scientific Research, Bangalore, India under the supervision of Prof. S. Balasubramanian and that it has not been submitted elsewhere for the award of any degree or diploma.

In keeping with the general practice in reporting scientific observations, due acknowledgement has been made whenever the work described is based on the findings of other investigators. Any omission that might have occurred by oversight or error of judgement is regretted.

Promit Ray

CERTIFICATE

I hereby certify that the matter embodied in this thesis entitled "**Computational Investigations on Carbon Dioxide Adsorption in Porous Framework Solids**" has been carried out by Mr. Promit Ray at the New Chemistry Unit, Jawaharlal Nehru Centre for Advanced Scientific Research, Bangalore, India under my supervision and that it has not been submitted elsewhere for the award of any degree or diploma.

Prof. S. Balasubramanian
(Research Supervisor)

Acknowledgements

Sincere respect and gratitude is due to my research supervisor, Prof. S. Balasubramanian. I owe the little knowledge in computational chemistry that I have almost entirely to him. I would like to thank him for his excellent advice not just as a guide but also as a mentor and friend. He will always be a source of inspiration. The academic freedom I received in his group has been liberating and I am indebted to him for it and the excellent computing facilities that he has provided for the group.

I am grateful to our chairman, Prof. C.N.R. Rao for giving me the opportunity to choose a field of my interest. Without his encouragement, I would have never been able to explore the intriguing field of computational chemistry.

I would like to thank the faculty members of NCU, CPMU, ICMS and TSU for all the courses they offered. I am particularly thankful to Prof. Swapan Pati, Dr. Jayanta Halar and Dr. Subi George for fruitful discussions. I have learned a lot from them.

JNCASR is acknowledged for providing state of the art research facilities. I acknowledge the Thematic Unit of Excellence in Computational Material Science (TUE-CMS) for providing excellent research ambience. I am particularly grateful to the open source community for providing useful software and operating systems. In particular, I would like to acknowledge the developers of LAMMPS, Gaussian09, CP2K and VMD.

I am grateful to all my past and present lab members - Dr. Anurag Sunda, Dr. Kanchan Sastri Palla, Dr. Sandeep K. Reddy, Pallabi Haldar, Rajdeep Singh Payal, B. Satyanarayana, Tarak Karmakar, B. Karteek, Anirban Mondal, Chaitanya Sharma, Sudip Das and Divyabharati for their company, help and support. They have maintained a wonderful work atmosphere.

I am grateful to B. Satyanarayana for helping me with large portions of the work presented here.

I would like to take this opportunity to thank all the people who have influenced me either directly or indirectly; friends, batchmates, acquaintances and mentors. Their company has been significant and I will always remember the good times with them.

Finally, I will always remain grateful to my parents for their constant support and encouragement throughout my life.

Preface

The thesis mainly deals with the computational study of porous solids which shows immense promise for carbon capture and storage (CCS). In particular, emphasis is placed on understanding CO_2 capture in ligand functionalized metal-organic frameworks (MOFs). An attempt is made to explore consequences of functionalization and optimization of porous materials through important case studies. Both classical and ab inito simulations have been used in these investigations.

Chapter 1 is a general introduction to CCS and the need to develop effective CO_2 capture strategies. It describes the current scenario of anthropogenic emission and the various methods of mitigation. This is followed by a discussion on various capture methods and commonly used materials. Apart from this, some fundamental points on classical and ab initio molecular dynamics simulation have also been mentioned here.

Chapter 2 deals with fluoro functionalized MOFs based on pyridinyl triazine and o-phthalic acid linkers. The o-phthalic acid linker can be functionalized in various ways and we consider MOFs based on fluorinated o-phthalic acid linkers. The focus of the chapter is to understand and explain unprecedented CO_2 capture and storage in these MOFs. This involves the presentation of some results of computational calculations and discussions on the conclusions drawn from the same.

Chapter 3 involves similar investigations on a series of Copper based MOFs with

hexafluorosilicate linkers. These structures form square shaped grids with commendable storage capacity. Quantum chemical calculations are performed to understand carbon capture in these MOFs. Finally, CO_2 uptake in these MOFs is modelled using classical methods.

Chapter 4 deals with azine functionalized frameworks. Ab initio calculations are performed to model the energetics of gas adsorption following which we use classical simulations to understand CO_2 uptake in these porous frameworks.

Contents

List of Figures

List of Tables

Chapter 1

Introduction

1.1 Carbon capture: The problem and the need to solve it

Carbon is an important component of biological systems and, therefore, the carbon cycle consists of a sequence of events that are undoubtedly the key in making the Earth capable of sustaining life.[1] Nature has maintained a fine balance in the total carbon content of the earth by distribution and exchange among the biosphere, pedosphere, geosphere, hydrosphere and atmosphere. About two-thirds of the total carbon on earth is stored inertly in the lithosphere in the form of fossil fuels, limestone rocks and sediments.[1] Such reserves of carbon are a result of storage over millions of years. The geological component of the carbon cycle operates slower in comparison to the other parts of the global carbon cycle. It is one of the most significant determinants of the amount of carbon in the atmosphere. Oceans contain the greatest quantity of actively cycled carbon.[1] Their surface layer holds large amounts of dissolved organic carbon that is exchanged rapidly with the atmosphere. The forms of carbon in the ocean include dissolved carbon dioxide gas; mostly as carbonates in seashells or the organic tissues of marine animals. Only about 1% of

the total carbon content is present in the atmosphere in two main forms: carbon dioxide and methane. Methane exists in much lower concentrations and is more short-lived than carbon dioxide.[2]

In the past two centuries, human activities have seriously altered the global carbon cycle. Fossil fuels - coal, oil and natural gas - currently provide for the explosively growing energy demands owing to increase in global population and industrialization. Combustion of these highly carbon-intensive resources involves production of a huge amount of carbon dioxide and its subsequent release in the atmosphere. As a result, humans have released several billion tonnes of carbon to the atmosphere in a span of about a hundred years.[3] Although carbon dioxide levels have changed naturally over the past several thousand years, human emissions of carbon dioxide into the atmosphere exceed natural fluctuations making it of critical importance to better understand how the carbon cycle works and what implications anthropogenic emission could have.

1.1.1 CO_2 as a greenhouse gas

A greenhouse gas absorbs and emits radiation within the thermal infrared range. Sunlight enters the Earth through the atmosphere. Subsequently, some gases in our atmosphere like carbon dioxide, methane and nitrous oxide trap some of the heat and keep the earth warm. This is the so-called greenhouse effect and is extremely important in maintaining temperatures on earth suitable for life forms. Without it, the average annual temperature of the earth would be nearly -17°C that would be too low for most living beings to survive. Greenhouse effect ensures that the temperature of the earth is maintained at 15°C and, therefore, makes it suitable for sustaining diverse forms of life. [4]

1.1.2 Temperature of the earth

The severe imbalance set in the carbon cycle due to the disproportionate release of CO_2 into the atmosphere has grave consequences. Research indicates that there has been a 40% increase in the atmospheric concentration of carbon dioxide since the onset of the industrial revolution from 280 ppm in 1750 to 392.6 ppm in 2012.[5] This increase has occurred despite the uptake of a large portion of the emissions by various natural "sinks" involved in the carbon cycle. This has possibly contributed to the increase in the average temperature on the surface of the earth. This global warming has led to the melting of ice-caps and glaciers in the poles, change in seasonal cycles and rise in sea-levels. This has dramatic detrimental consequences on various biological ecosystems. Effective techniques to reduce CO_2 emission are thus urgently needed to maintain the global climate and to protect our environment.

1.2 Carbon capture and storage : Sequestration of CO_2

A promising approach to mitigate CO_2 emission is carbon capture and storage (CCS) which involves trapping and removal of gaseous CO_2 from the atmosphere. This is a complex task that can be roughly divided into two: (i) capturing CO_2 from the dilute gas streams and (ii) storage of the captured CO_2. Storage is envisaged either in deep geological formations or the form of mineral carbonates. Permanent storage of CO_2 using methods of sequestration is discussed. These methods lay emphasis on long-term storage of atmospheric CO_2. Sequestration can be of the following types

-

1. Biological Sequestration
2. Physical Sequestration

3. Chemical Sequestration

1.2.1 Biological Sequestration

Biosequestration attempts to sequester carbon through biological processes that affect the global carbon cycle since these processes created fossil fuels. By manipulating such processes, geoengineers seek to enhance sequestration.

Reforestation

Plants remove CO_2 from the atmosphere for photosynthetic activity and, therefore, this removal can be increased manifold through reforestation. Forests, therefore, function as 'terrestrial carbon sinks'. Anthropogenic emissions can thus be reduced through forestry activities via four major strategies -
(i) bringing more land under forests to increase the amount of forest cover. (ii) increasing the carbon density of existing forests. (iii) forest products could be developed and used to reduce the dependence on fossil fuels and (iv) subsequent reduction in carbon emissions as a result of deforestation and degradation.[6] There are a number of factors to be considered about the reforestation issue. Planting trees anywhere and everywhere will not necessarily help in mitigating emission. It has been found through extensive research that large reforestation in the Arctic or sub-arctic regions will interfere with the reflection of heat from the thick snow cover and thus won't contribute to the reduction of global warming. Again, planting trees in the temperate latitudes would have a net warming effect on the atmosphere as the heat released by the leaves is much more than they absorb. Essentially, reforestation in the tropical latitudes could lead to the desired effect through the formation of clouds that would reflect the sunlight and reduce the heat. [6,7]

Agriculture

Agricultural practices can be significantly modified such that there is a minimisation in the release of carbon dioxide to the atmosphere. Mitigation of carbon emissions could be achieved in two ways: (i) practices to reduce emissions of greenhouse gases into the atmosphere and (ii) enhancing carbon removal. Efficient agricultural practices that are less energy intensive like no-till farming not only reduces the release of carbon trapped in the soil but the soil performs as a better carbon sink. Use of cover crops is of interest in sustainable agriculture and can reduce greenhouse emissions considerably. [8]

Involvement of agricultural methods that return the biomass to soils can help achieve the second goal. Use of cover crops between planting seasons, restoration of degraded land and enhancement in the water-retaining capacity of the soils to enhance the growth of carbon-capturing microbes are some of the commonly adopted approaches.

Apart from these, other biological sequestration techniques include peat production and wetland restoration.

1.2.2 Physical Sequestration

Bio-energy with carbon capture and storage (BECCS)

BECCS refers exclusively to the combustion of biomass for energy, the CO_2 emissions from which are captured. It is a method that produces negative carbon dioxide emissions by combining the use of bioenergy with geologic carbon capture and storage. The concept is drawn from the integration of trees, use of this biomass and subsequent capture and storage so that there is a net reduction in the amount of atmospheric carbon dioxide. [9]

Bio-char

Biochar is a special type of charcoal created by pyrolysis of biomass. It helps in mitigating carbon dioxide emissions because it acts as a carbon sink enhancing negative carbon emissions and is also as an alternate energy source. [10]

1.2.3 Chemical Sequestration

Converting CO_2 chemically into less harmful chemical species for storage is currently one of the most widely accepted and explored methods of mitigating carbon based emissions. This process involves reacting the captured CO_2 with amines or metal oxides to form stable carbonate minerals.

Chemical Scrubbers

These devices trap exhaust fumes from industrial plants and treat individual gases so as to remove the harmful contents in these fumes. Examples include amine scrubbers and activated carbon.[11] Other processes involve injecting CO_2 into deep-sea formations so that it reacts with the basalt and thus forms stable carbonate minerals. Secondly, carbon dioxide forms carbonic acid whenever it dissolves in water. The resulting ocean acidification prevents further absorption of atmospheric carbon dioxide. Adding bases like crushed limestone and sodium hydroxide could aid in the neutralization of sea water. [12]

1.3 Carbon capture and storage : capture of CO_2

It must be mentioned that the aspect of CCS discussed thus far is less challenging because transportation and storage of CO_2 are relatively mature technologies. Most of the cost-intensive and challenging problems are encountered in the CO_2 capture

step, and that is the main focus here.

1.3.1 Capture strategies and costs involved

It is important to realize that the choice of strategy and materials for capture depends strongly on the generation of CO_2 in terms of temperature, pressure, concentration and the nature of other gases in the mixture. Depending on the fundamental chemical processes involved in the combustion of fossil fuels, the three most common strategies are:[13] (i) postcombustion, in which CO_2 is removed from flue gas generated by burning fossil fuels in air. It is expensive because a dilute CO_2 stream (10-15 % by volume) has to be separated from N_2 yet the most feasible on a short time scale because the proposed technologies can easily be fitted to an existing power plant. (ii) Precombustion, which involves the reaction of a fuel with a controlled amount of O_2 to yield CO and H_2 which is further reacted with steam to give CO_2 and H_2. Separating a denser stream is easier and less expensive. (iii) Oxycombustion, where fossil fuels are burned in pure oxygen; the advantage being that the gaseous product is exclusively CO_2 which can be directly stored. This has the requirement of nearly pure oxygen which can be expensive in itself. An appropriate technology has to be selected on the basis of both ease of capture as well cost of implementation. Postcombustion capture involves an expensive capture step, but it also involves the most economical and tried strategy towards energy production. Therefore, selection of a suitable carbon capture strategy is not a trivial task.

1.3.2 Technologies and materials commonly explored for CO_2 capture

The fundamental factor in material choice should be higher affinity of the material for CO_2 than other gases present in the mixture. This could be based on absorption, adsorption or selective permeability.[14] Binding can be physical which is temperature

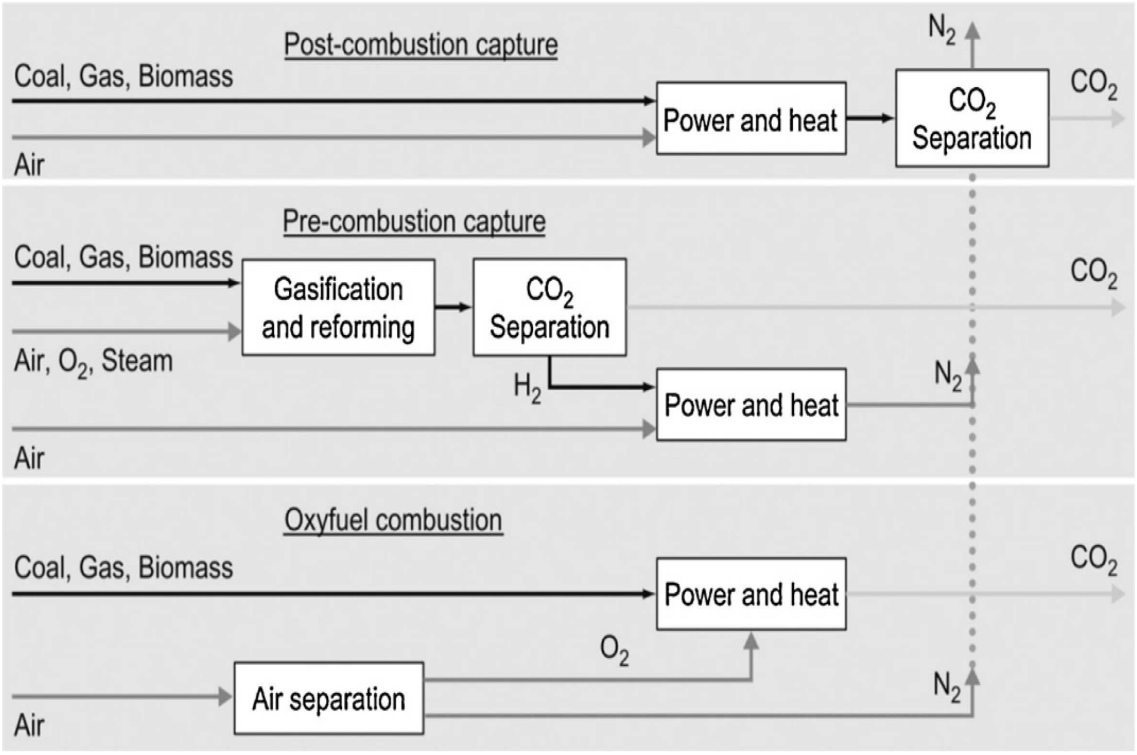

Figure 1.1: Three common strategies of capturing CO_2 from power generation plants.[13]

and pressure dependent or chemical where it would depend on the extent of the chemical interactions. Chemical binding is usually associated with strong affinity and, therefore, regeneration of the solvent is energy intensive. Common media are solvent absorbents. Absorption is a well-established separation technique in this category used most commonly as 'amine scrubbing'. Typical solvents used are amines such as monoethanolamine and ammonia solutions. Membranes have great potential for precombustion capture, and common media include polymeric and ceramic membranes. Membrane separation is based on selective permeability on the basis of differences in physical or chemical interactions between gases and the membrane material. Physical binding usually results in weak affinity, but the surface of the material can be coated or functionalized to enhance binding. Therefore, regeneration of the solvent is not expensive. Typical media include nanoporous solid adsorbents such as zeolites and layered clays and solvents such as ionic liquids and selexol. Ionic liquids are a recent addition to the list that have shown potential

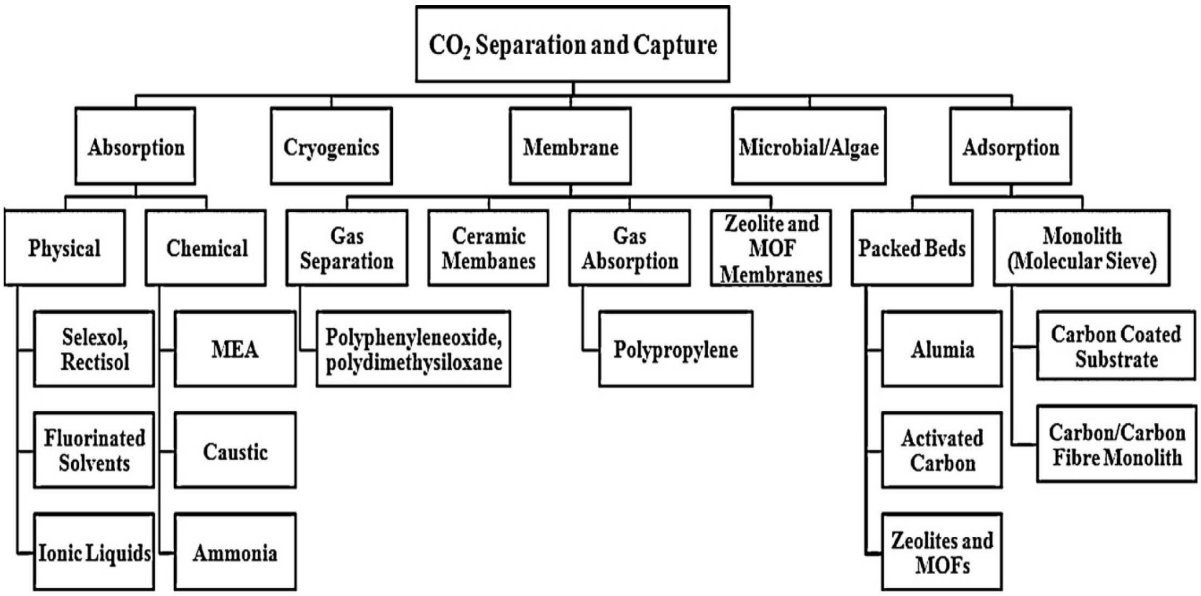

Figure 1.2: Different technologies and typical materials for CO_2 capture and storage.[13]

for absorption of CO_2 and are environmentally benign. Gas separation based on adsorption has been well developed, but there is still plenty of room to optimize the adsorption ability of these materials and explore new sorbents. In the past two decades, there has been a lot of interest in a new class of porous materials: metal-organic frameworks (MOFs). The work in the thesis deals with the simulation of CO_2 adsorption in MOFs and, therefore, the subsequent paragraphs deal with MOFs, the interest and prerequisites for simulation of gas uptake in MOFs.

1.4 Metal-organic frameworks (MOFs)

Metal-organic frameworks are a new class of porous crystalline materials that are composed of ordered networks containing two constituents, metal ions and organic linkers.[15] MOFs are geometrically and crystallographically well-defined structures consisting of metal ions or clusters coordinated to rigid organic molecules to form one, two, or three-dimensional structures that can be porous and extend infinitely in three directions. In other words, a MOF is a coordination network with organic ligands

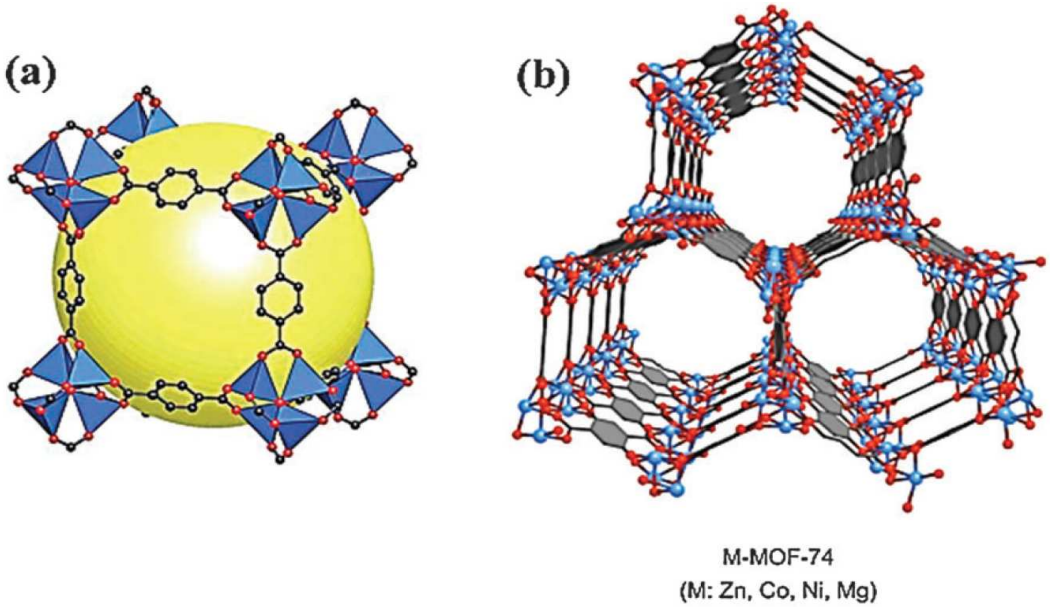

Figure 1.3: Structures of two MOF examples. (a) IRMOF-1. SBU: ZnO_4 tetrahedron, ligands: terephthalic acid, black balls: C atoms, red balls: O atoms, yellow sphere: center cavity. (b) M-MOF74. M = Zn, Co, Ni or Mg, blue balls: metal atoms, red balls: O atoms, gray stick: C atoms.[15]

containing potential voids. In some cases, the pores are stable during elimination of the guest molecules which are often solvents. Due to their unique properties, they have found applications in catalysis, sensing and separation, gas storage, drug delivery, luminescence, magnetism, non-linear optics and molecular recognition. They can be easily prepared under mild conditions. The structure of MOFs containing metal ions and ligands can be determined using X-ray crystallography. Transition metal ions are often used and depending on their oxidation state and coordination number, many coordination environments can be obtained, some of which are linear, T or Y-shaped, tetrahedral, square-planar, square-pyramidal, trigonal-bipyramidal, octahedral, trigonal-prismatic, pentagonal-bipyramidal and their distorted forms. MOFs are categorized into three classes: (i) first generation MOFs which are microporous in nature and collapse irreversibly upon guest removal. (ii) second generation MOFs which are robust and rigid frameworks that maintain their crystalline nature even after the removal of guest molecules and (iii) third generation MOFs which

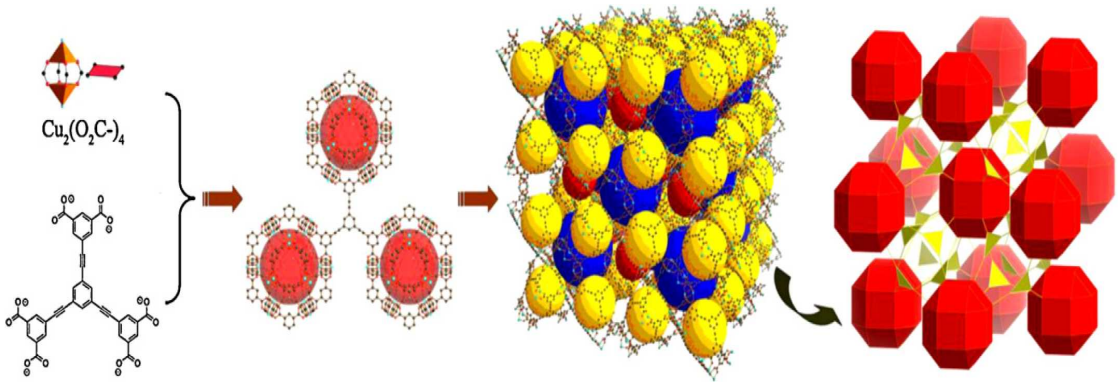

Figure 1.4: Construction of a designed MOF, from metal-containing node and bridging organic ligand to supramolecular building unit and then to three-dimensional porous framework. The last image highlights the geometrical assembly of the framework.[13]

are flexible and dynamic frameworks, which respond to external stimuli such as temperature, pressure and guest molecules in a reversible manner. Rigid MOFs have frameworks with permanent porosity whereas flexible MOFs possess dynamic frameworks that are stimuli responsive. This sensitivity results in special properties such as pressure or temperature dependent molecular sieving, something that is well beyond the reach of traditional adsorbents such as zeolites and activated carbons. MOFs can be designed conceptually based on how the constituent building blocks come together to form a net.[13] Therefore, the structures and properties of MOFs are easily tuned by intelligent choice of building blocks. This remarkable and easy tuning gives MOFs a significant advantage over traditional porous materials. It allows excellent optimization of pore dimension, surface properties and other factors for specific applications as a porous material. MOFs with very high porosity can be synthesized typically by a self assembly reaction between metal ions and organic linkers. MOFs hold several records in porous materials including highest surface area, hydrogen uptake, methane and CO_2 storage.

1.4.1 Ligands in MOFs

As shown in Figure 1.5, organic molecules with specific functional groups are used as ligands for MOF synthesis. Multidentate bridging ligands with two or more linking sites or donor atoms are commonly used in the synthesis of MOFs thus resulting in unique binding strength and topology. Physical properties are strongly dependent on the length of the ligand as well as number and nature of binding sites and, therefore, can be tuned by modifying the organic ligand. Ligands with carbon, oxygen or nitrogen are generally used in MOF synthesis. The metal coordination number can be controlled to be less than its full valence by careful choice of ligands and linking sites. This allows the dimensionality of the MOF to be tuned to result in different desired topologies and physical properties. Carboxylate ligands tend to form more stable frameworks because of strong electrostatic interaction and chelation effect. Functionalizing ligands to enhance interaction between linkers of the MOF and adsorbed gases has emerged as a new technique and has received much attention. There could be two problems associated with using organic linkers: (i) linkers which exhibit more than one conformation could lead to unpredictable structures. With such linkers, different crystal structures can be observed by simply changing the concentration of reactants, type of anion, temperature, etc. To overcome these problems, ligands with rigid backbones such as 4,4-bipyridine, 2,4,6-tri-4-pyridyl-1,3,5-triazine, etc. have been introduced that restrict the orientational freedom of ligand lone pairs. (ii) Large bridging ligands lead to networks with large cavities and these networks interpenetrate so that the resultant cavity size is drastically decreased. Strategies proposed to overcome this problem include use of charged frameworks, bulky ligands and secondary building units, as well as increase of binding between guest molecules and framework.

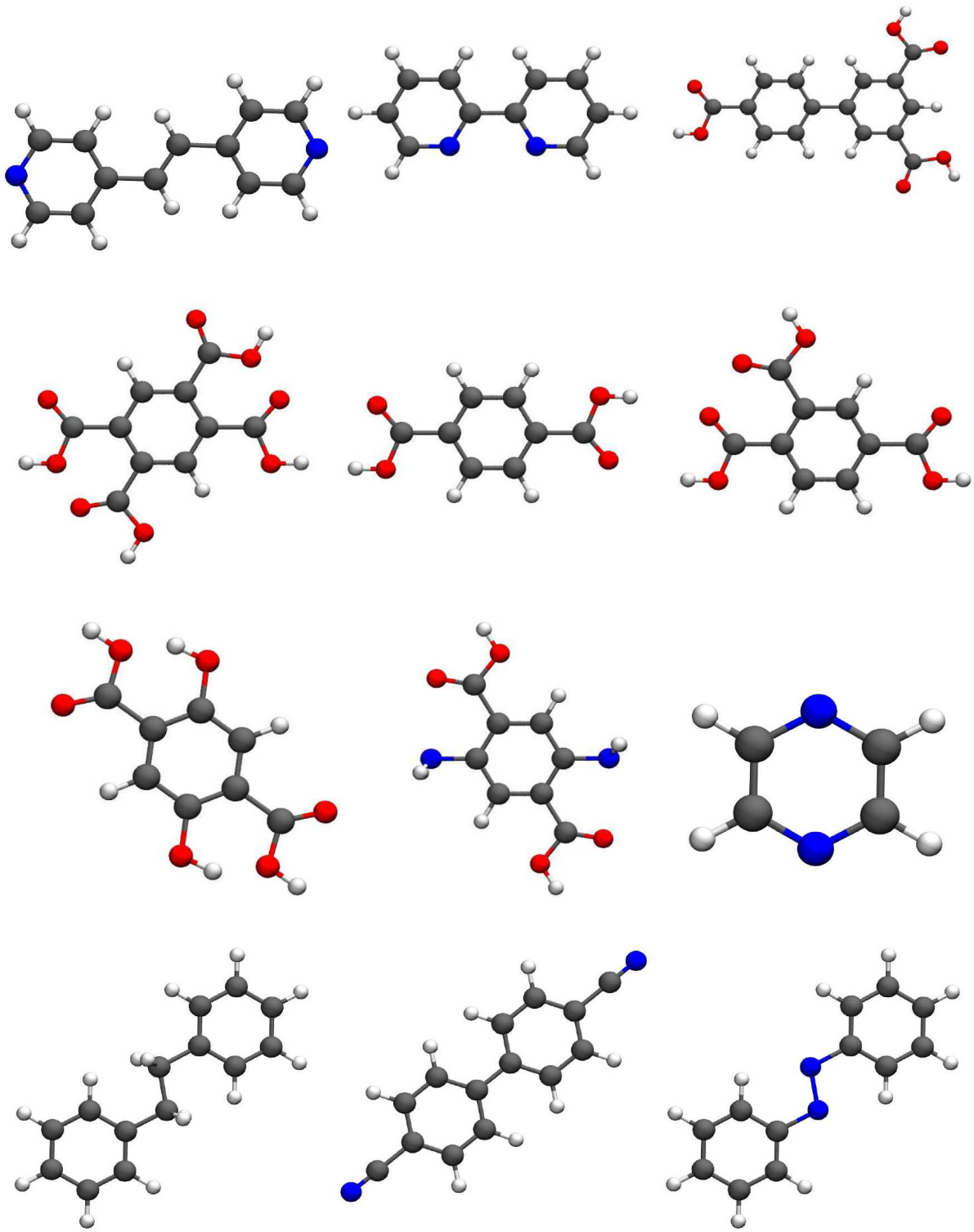

Figure 1.5: Examples of common ligands used. Colour code: C, grey; O, red; N, blue; H, white.

1.4.2 Properties and applications of MOFs

MOFs have applications in diverse areas owing to their unique properties. Some of them are briefly discussed here: (i) due to their extremely high surface areas and pore volumes, they can be used for capture and storage of gases such as carbon dioxide, hydrogen, methane, nitrogen, etc. Among these, MOFs have been shown to exhibit considerable promise for hydrogen and methane storage. The gases once captured can be released either by increasing temperature or decreasing pressure. The functionalization of pore surface allows one to tune adsorption capacity and heats of adsorption. These MOFs can be used to transport or store gases for clean energy applications. The thesis deals with the simulation of CO_2 adsorption in MOFs and, therefore, this aspect is discussed in some detail in the next section. (ii) MOFs show gas or liquid selectivity due to molecular sieving and selective adsorption. Gas selectivity is typically related to the size of the guest molecule, pore size and surface chemistry while liquid selectivity depends on specific guest-host and guest-guest interactions. Selectivity values are temperature and pressure dependent. (iii) Since there is no limitation on pore size unlike zeolites, MOFs have numerous catalytic applications. They provide homogeneous surface due to high crystallinity. Few strategies have been proposed for engineering MOFs specifically for catalytic applications, and these are just mentioned here. (a) Framework activity. (b) Encapsulation of active species into the pores. The MOF interacts with these through non-covalent interactions. (c) Post-synthetic modification to introduce functional groups and metal complexes. The active species interact with MOF through covalent interactions. The major disadvantage of these materials for catalytic applications is the issue of stability under different environments and the associated cost.

1.4.3 CO_2 storage

The prime advantage of using MOFs over other materials for carbon capture is the ease of desorption. The amount of energy required for heating the adsorbent to release the adsorbate molecules is comparatively less, and this significantly reduces the energy cost associated with desorption. In situ vibrational spectroscopy, computational methods and crystallographic methods aid in understanding the locations of CO_2 molecules inside the framework. These methods also help in identifying the portions of a MOF that are responsible for material performance regarding gas storage and, therefore, it is possible to enhance its performance by rational modification of the structure. Several features of MOFs determine their success in carbon capture and a few are briefly mentioned here. Adsorption capacity is a critical parameter selection and design of the MOF for CO_2 capture and storage. High volumetric and gravimetric uptake are both important in CO_2 storage. The chemical nature of the pore surface dictates interaction with adsorbents and, therefore, tunes the adsorption capacity of MOFs. One can predict gas storage capacity of various MOFs depending on the nature of binding sites and their number within the pore. It has been shown that fluorination of ligands and pendant alkylamine functionalities incorporated into the pores are effective ways to achieve enhanced adsorption. Heat of adsorption dictates the affinity of the pore surface towards CO_2 selectivity, the binding energy and subsequently, the energy cost associated with desorption process. Extremely high binding energies result in a huge energy cost required to release the gas. If the heat of adsorption is too low, it affects CO_2 selectivity and uptake. Therefore, moderate values for heat of adsorptions of CO_2 are ideal for economical purposes, and these can be obtained easily with the functionalization of pore surface without changing the backbone structure. Since flue gas is a mixture of more than two gases, high selectivity for CO_2 gas is required for practical applications. Since MOFs, which show high surface areas and pore volumes possess pore sizes larger

than the size of gas molecules, the CO_2 selectivity is defined by adsorption sites in the pore. Many MOFs are not extremely stable against water vapour due to high metal content. This observation hinders many reported MOFs from being used for CO_2 capture from flue gas.

1.5 Role of molecular simulations

Computer simulations shed light on the microscopic details involved at the interface of gas and MOF. This knowledge can be used to design new MOFs and tune existing MOFs for specific applications. Importantly, the location of gas molecules inside the MOF is difficult to obtain experimentally. Often, the MOF turns into a polycrystalline powder upon desolvation, and it is nearly impossible to obtain coordinates of atoms from X-ray diffraction of the powder sample. Thus, one has to use local probes such as vibrational spectroscopy and NMR to identify their locations. Simulations can easily identify locations of gas molecules and their interactions sites within the framework. In this manner, the combination of both experiments and computer simulations allows one to design high-performance MOFs. Simulations require the modelling of both adsorbate and adsorbent. There are two methods to study these interactions - classical and ab initio.

1.5.1 Scope of classical simulations

Classical force fields allow one to study large systems in a relatively lesser time provided force field parameters are available. In most cases, the framework is considered to be rigid, and this avoids the need to develop intramolecular parameters for adsorbent. Lennard-Jones (LJ) parameters are taken from general all-atom force fields such as UFF,[16] OPLS-AA,[17] DREIDING,[18] etc. with charges for electrostatic interactions derived from quantum mechanical calculations. Alternatively, LJ potential

alone is used, and the electrostatic contributions are assumed to be either negligible or are effectively included in the LJ parameters. One of the main challenges in understanding the diffusion of gases in MOFs is the lack of experimental information on transport properties. Thus far, molecular dynamics (MD) is the main technique that has been used to investigate kinetic properties of gases in MOFs. MD has been employed to study CO_2 diffusion in MOFs as this is crucial to evaluate the overall performance of the MOF. Adsorption isotherms of pure gas or mixtures can be calculated using simulations carried out in the grand canonical Monte Carlo (GCMC) ensemble. GCMC has been one of the most extensively used methods to understand gas uptake in MOFs. It allows the fluctuation of the number of particles that exactly resembles the experimental conditions. However, it is to be mentioned that the calculated adsorption characteristics of MOFs do not always match with experiments. Possible reasons for this include (i) inaccurate force field (ii) errors in synthesis leading to defects (iii) improper activation of MOF and (iv) MOF flexibility. Monte Carlo method can also be used to calculate selectivities, surface areas and heats of adsorption. Experimentally, the former is calculated from N_2 adsorption measurements using BET theory. Both MD and GCMC calculations have been utilized to model adsorption in various MOFs in this work.

1.5.2 Quantum mechanical calculations

Quantum mechanical calculations include electron-electron and electron-nucleus interactions explicitly in the simulations and, therefore, these are parameter-free (at least, in principle) and provide accurate interaction energies between the adsorbate and adsorbent. These are generally used to find locations of adsorbates inside the framework and their interaction energies. *Ab initio* calculations are expensive and normally implemented when detailed information regarding physical and chemical interactions is required. Density functional theory calculations have been used from

small clusters to large systems because of the computational efficiency. However, DFT has some deficiencies such as consideration of dispersion interactions. In general, *ab initio* calculations can be carried out by considering either the entire crystal (periodic calculations) or a specific part of it (cluster or fragment calculations). In the former, Kohn-Sham DFT calculations augmented with van der Waals interaction terms are widely used while in the latter, wave function based methods such as second order Moeller-Plesset perturbation theory (MP2), coupled cluster techniques (CCSD), etc. have also been employed. Here, we restrict ourselves to methods based on DFT and illustrate the use of these advanced techniques to obtain a microscopic understanding of gas adsorption.

1.6 Molecular dynamics

Molecular dynamics is a numerical technique used to calculate forces acting on the atoms of the system. This is nothing but the negative gradient of potential energy with respect to the atom position. MD can be broadly classified into two branches - classical MD and ab initio MD. In classical MD, the potential is a function of the atomic coordinates only, whereas, in ab initio MD, the potential is a function of both the electronic and nuclear coordinates.

1.6.1 Classical Molecular Dynamics

In classical MD, Newton's equation of motion are solved for computing the equilibrium and transport properties of a classical many body system. The classical equations of motion for a simple atomic system are given as -

$$\mathbf{f_i} = m_i \ddot{\mathbf{r}} \tag{1.1}$$

where $\mathbf{f}_i$ is the force acting on i^{th} particle, m_i is the mass of the i^{th} particle and $\ddot{\mathbf{r}}$

denotes the acceleration of the i^{th} particle. The force acting on the i^{th} particle is related to the potential energy of the system, U as -

$$f_i = -\frac{\partial U}{\partial r_i} \tag{1.2}$$

For a system consisting of N particles, the total potential energy of the system is given as $U(r^N)$ where $r^N = (r_1, r_2, ...r_N)$ denotes the 3N coordinates of all the N particles in the system. There are two major contributions to the total potential energy of the system - energy from the bonded interactions (or, intramolecular interactions), U_b and the energy from the non-bonded interactions (or, inter-molecular interactions), U_{nb}.

The intramolecular energy, U_b can be written as a sum of the contributions from bond stretches - U_{bonds}, angle flexing - U_{angles}, torsional rotations - $U_{dihedral}$ and improper interactions - $U_{improper}$. This is given as -

$$U_b = U_{bonds} + U_{angles} + U_{dihedral} + U_{improper} \tag{1.3}$$

The intermolecular energy, U_{nb} is given as the sum of 2-body, 3-body,..., N-body terms as-

$$U_{nb}(r^N) = U_{2body} + U_{3body} + ... + U_{Nbody} \tag{1.4}$$

In most calculations, three-body and higher terms are neglected as they are expensive to calculate. It is only the two-body interaction term, also known as pair-potential, which is considered for most practical purposes. One of the most commonly used pair-potential forms is the Lennard-Jones potential,v^{LJ}, which is written as,

$$v^{LJ} = 4\epsilon \left[\left(\frac{\sigma}{r} \right)^{12} - \left(\frac{\sigma}{r} \right)^{6} \right] \tag{1.5}$$

The Lennard-Jones potential contains two important parameters - σ, the diameter and ϵ, the well depth. r is the pair-wise distance. The electrostatic interactions are calculated using Coulomb potential,$v^{Coulomb}$, as -

$$v^{Coulomb}(r) = \frac{Q_1 Q_2}{4\pi\epsilon_0 r} \tag{1.6}$$

where Q_1, Q_2 are the charges of the two interacting molecules, r is the pair-wise distance and ϵ_0 is the electrical permittivity of the space.

Force-field is a description of the potential energy of the system, containing the values of the set of bonded and non-bonded parameters to perform MD on the system. Hence, this is used to calculate the forces on the system using that specific potential form.

1.6.2 Ab initio Molecular Dynamics

There are certain drawbacks of classical Molecular Dynamics which limit its applications. The major limitation is that the results are dependent on the extent of perfection of the model used. The more perfect the model, the more perfect is the description of the system. But, determining a new potential form for a new complex system with many interactions is a challenging task and more prone to human limitations. Another problem is the transferability of such potentials.

Ab initio molecular dynamics deals with the calculation of electronic degrees of freedom. This method exploits the Born-Oppenheimer approximation that solves the electronic Schrödinger equation for a given nuclear configuration. Analogous to Classical Molecular Dynamics where the forces on each particle are calculated by solving Newton's equations of motion, here, at first, the electronic distribution in the ground state is determined from the Schrödinger's equation after which, the forces are calculated by using Hellmann-Feynman theorem.

According to Bloch's theorem, each electronic wave function can be expressed as a sum of plane waves as -

$$\psi_i = \sum_k C_k^i e^{veck,vecr} \tag{1.7}$$

where the coefficients of expansion are $C_k{}^i$'s. The electronic wavefunction can be expressed by a complete set of coefficients, denoted by C. Thus, it can be seen that for condensed phases, the wave-function consists of two parts - a periodic part and a phase factor. The periodic part is expressed by plane waves basis-sets.

Density Functional Theory

Another important concept widely used in ab initio Molecular Dynamics is Density Functional Theory. This theory essentially relies on two theorems - the Hohenberg-Kohn Theorems. The first theorem expresses the ground-state wavefunction as a function of the ground-state electron density, as -

$$\psi_0 (r_1, r_2, ...r_N) = \psi [n_0 (r)] \tag{1.8}$$

Here,ψ_0(r) represents the ground state wavefunction and n_0(r) represents the ground state electron density. So, it directly follows from this, the expectation value of any ground state observable $\hat{O}$ is a functional of ground state electron density n_0(r),as -

$$O_0 = O[n_0] = \langle \psi[n_0|\hat{O}|\psi[n_0] \rangle \tag{1.9}$$

The second theorem deals with the calculation of ground state energy. This energy is expressed as -

$$E_{v,0} = E_v[n_0] = \langle \psi[n_0]|\hat{H}|\psi[n_0] \rangle \tag{1.10}$$

where the total Hamiltonian is expressed as a sum of Kinetic energy(T) and Potential

Energy(U+V) as $\hat{H} = \hat{T} + \hat{U} + \hat{V}$. Similar to the variational theorem, the ground state energy has the variational property, as

$$E_v[n_0] \leq E_v[n^{'}] \tag{1.11}$$

This implies that the energy corresponding to any wavefunction ψ which is not equivalent to the ground state wavefunction ψ_0, will always be greater than the ground state energy. [19]

Pseudopotentials

The electronic states of an atom are essentially divided into three parts - (a) *core-states* (b) *valence-states* and (c) *semi-core states*. *Core-states* refer to the innermost electronic states of the atom, which do not participate in bonding. *Valence-states* refer to the outermost electrons that participate in chemical reactions. *Semi-core states* are those states that are mostly localised and do not have a direct contribution to chemical bonding. So, in actual calculations, there is no strict necessity for a precise description of the inner electrons inside the core. That brings us to the concept of a pseudopotential which is an approximation for the inner orbitals to be replaced by a smooth, nodeless pseudo-wavefunction. When this potential replaces the actual potential, we have a pseudo-atomic problem that is not wrong but easier and faster to solve. So, pseudopotential function is extensively used in ab initio calculations.

1.7 Scope of the thesis

The thesis deals with an issue of currrent interest and importance in the scenario concerning anthropogenic emission. Intelligent design of optimized porous materials requires significant input from theoretical studies ranging from simulated uptake

to estimates of enthalpies of adsorption. The MOFs modelled in this thesis show exceptional carbon capture potential and are typically obtained through delicate functionalization of the ligands in the linkers. The thesis aims to elcidate possible interactions leading to enhanced storage as well model the uptake of CO_2 by these porous frameworks to reproduce experimental data. It is believed that careful study of porous materials from a theoretical point of view will assist further synthesis of materials with excellent gas storage abilities.

Bibliography

[1] Falkowski, P. et al. *Science* **2000**, *290*, 291–296.

[2] Forster, V. e. a., P.; Ramawamy *Changes in atmospheric constituents and in radiative forcing*; Cambridge University Press, Cambridge, 2007.

[3] Crowley, T. J. *Science* **2000**, *289*, 270–277.

[4] `http://www.undeerc.org/PCOR/Sequestration/greenhouseeffect.aspx`.

[5] `http://www.cdiac.ornl.gov/pns/current_ghg.html`.

[6] Canadell, J. G.; Raupach, M. R. *Science* **2008**, *320*, pp. 1456–1457.

[7] Silver, W. L.; Ostertag, R.; Lugo, A. E. *Restoration Ecology* **2000**, *8*, 394–407.

[8] `http://www.scielo.br/scielo.php?pid=S0103-90162009000200013{\&}script=sci_arttext`.

[9] `http://citeseerx.ist.psu.edu/viewdoc/download?doi=10.1.1.231.3339{\&}rep=rep1{\&}type=pdf`.

[10] Badger, P. C.; Fransham, P. *Biomass and Bioenergy* **2006**, *30*, 321 – 325, Proceedings of the third annual workshop of Task 31 'Systainable production systems for bioenergy: Impacts on forest resources and utilization of wood for energy' October 2003, Flagstaff, Arizona, {USA}.

[11] Rochelle, G. T. *Science* **2009**, *325*, pp. 1652–1654.

[12] Harvey, L. D. D. *Journal of Geophysical Research: Oceans* **2008**, *113*, n/a–n/a.

[13] Li, J.-R.; Ma, Y.; McCarthy, M. C.; Sculley, J.; Yu, J.; Jeong, H.-K.; Balbuena, P. B.; Zhou, H.-C. *Coordination Chemistry Reviews* **2011**, *255*, 1791 – 1823.

[14] Maiti, A. *International Journal of Quantum Chemistry* **2014**, *114*, 163–175.

[15] Liu, J.; Thallapally, P. K.; McGrail, B. P.; Brown, D. R.; Liu, J. *Chem. Soc. Rev.* **2012**, *41*, 2308–2322.

[16] Rappe, A. K.; Casewit, C. J.; Colwell, K. S.; Goddard, W. A.; Skiff, W. M. *Journal of the American Chemical Society* **1992**, *114*, 10024–10035.

[17] Jorgensen, W. L.; Tirado-Rives, J. *Journal of the American Chemical Society* **1988**, *110*, 1657–1666.

[18] Mayo, S. L.; Olafson, B. D.; Goddard, W. A. *The Journal of Physical Chemistry* **1990**, *94*, 8897–8909.

[19] `arXiv:cond-mat/0211443`.

Chapter 2

Modelling CO_2 adsorption in the fluorinated TKL MOFs

2.1 Introduction

The pressing need to check anthropogenic emission of CO_2 has recently led to an enormous interest in the functionalization and optimization of novel porous materials for carbon capture and storage (CCS). CCS is a reasonably viable strategy and shows huge promise for mitigation of CO_2 emission at an industrial level. Towards this goal, there has been much attention focussed on developing materials for CO_2 removal at low concentrations to facilitate easy capture from flue gas streams. In particular, crystalline porous solids are ideal candidates for efficient low concentration carbon capture. Among these materials, MOFs possess tunable properties that allow easy manipulation of their pore architecture and, therefore, they have been widely explored for these applications over the past two decades. Although the large surface area may facilitate high gravimetric uptake of gases at low temperature or high pressure, it is not necessarily conducive for efficient separations under practical

and ambient conditions. Moreover, the ability of MOFs to remove trace concentrations from gas streams has been relatively less explored. This lack of investigation is mainly because most of the MOFs reported so far show comparatively poor uptake and selectivity at ambient conditions. In fact, there are very few MOFs reported so far which exhibit over 100 cubic centimetres per gram CO_2 uptake at 298 K and 1 atm. The urgent need of the hour, therefore, is to tailor the kinetics and thermodynamics of gas adsorption with precise control over pore size and functionality for use in CCS. Ligand functionalization has been proven as an efficient way to regulate the affinity between adsorbed gases and the host framework without causing significant distortion in the structure of the latter. Recently, the utilization of alkylamine and fluorinated linkers to decorate the surface of MOFs has caught a lot of attention. It has been reported that fluorous MOFs (FMOFs) can show remarkable gas adsorption properties due to enhanced interactions between the fluorinated pore surface and CO_2 molecules. However, it is also observed that fluorination of ligands does not always result in high CO_2 adsorption capacities. Enhancement of adsorption is rather system-specific and in some cases, gas adsorption of the desired MOFs had no obvious increase or had even decreased. This can be explained on the basis of changes in pore structure caused upon fluorination; the free pore volume may be effectively reduced by the inserted functional groups. Therefore, the effect of fluorination in MOFs towards gas adsorption is only vaguely understood and systematic studies are required to achieve performance targeted rational design and synthesis. It thus becomes important to understand from a theoretical standpoint, the interactions between the adsorbed CO_2 and the fluorinated linkers of the MOF and how these might affect adsorption properties. This knowledge also helps in understanding the differences in pore architecture and size inherent in the topology of the FMOFs. Further, high adsorption capacity of MOFs is often associated with high heats of adsorption owing to strong interactions between the adsorbate and the guest molecule.

However, experimentally obtained isosteric heats for CO_2 adsorption show several anomalous trends that are not easy to understand from the pore architecture and functionality of the framework alone. These need to be understood by considering various CO_2-adsorbate interactions and chemical environments around each of the individual binding sites. Here, we model CO_2 adsorption in a family of FMOFs that show unprecedented CO_2 uptake under ambient conditions with emphasis on adsorption sites and trends in isosteric heat.

It has recently been found that the reaction of Ni(II) ions with 2,4,6-tri(4-pyridinyl)-1,3,5-triazine (tpt) and o-phthalic acid (OPA) could result in highly porous frameworks.[1] Choice of o-phthalic acid as co-ligand allows easy functionalization of pore surface and subsequent tuning of adsorption properties. The TKL (TKL = Tianjin Key Lab of Metal and Molecule Based Materials) series of MOFs has thus been reported by functionalizing the OPA ligand with nitro, amino and fluoro groups. Among these, we consider three FMOFs showing the highest CO_2 uptake in the series (TKL-105, 106 and 107) for simulations. These vary in the number and position of substituted fluorine atoms on the OPA ligand but all three show high surface areas and excellent ability for CO_2 capture. The focus here is to predict likely adsorption sites and corresponding energies of adsorption. Apart from elucidating the microscopic nature of interactions between the gas molecules and framework, an effort is made to look at the architecture of the binding sites in detail in each of the MOFs to explain anomalous trends in the isosteric heats which in turn influences uptake dramatically.

In the following, classical molecular dynamics simulations have been used to study diffusion of CO_2 in these MOFs and locate binding sites quickly by sampling the entire space within. Ab initio methods are then used to explore regions near functional groups and predict the influence of the chemical environment around the

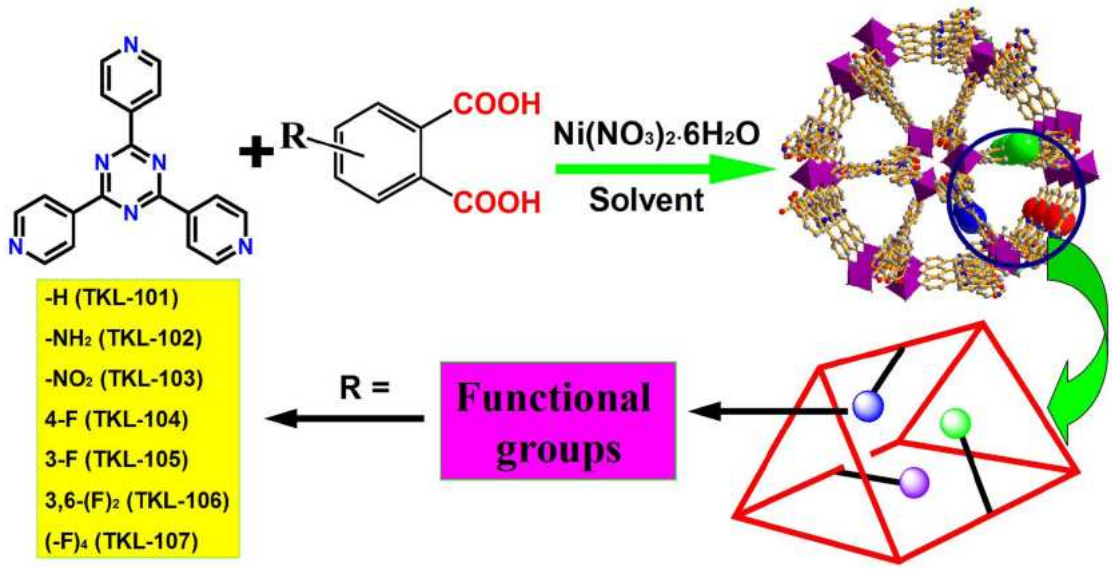

Figure 2.1: Scheme of TKL MOFs. Reproduced with permission.[1]

binding sites on adsorption enthalpies. The MOFs in consideration have very similar structures and, therefore, also have equivalent binding sites with almost identical binding energies. Presumably the drastic differences in uptake and enthalpies observed experimentally arise because of delicate effects of fluorination and we try to understand these aspects here. In particular, TKL-107 shows a very low isosteric heat that increases with loading in contrast to the other MOFs but surprisingly, it also shows the highest uptake in the series. These seemingly contrasting trends are central to ligand functionalization and, therefore, a thorough understanding is essential to motivate rational design in the future. This work attempts to address these issues.

The experimentally obtained structures of these MOFs are used as a starting point in these calculations after elimination of solvent molecules. An effort is also made to investigate the effects of desolvation. However, we calculate all binding energies using desolvated structures. TKL-107 has all four positions on the OPA ligand substituted while TKL-106 has two equivalent positions substituted. TKL-105 is

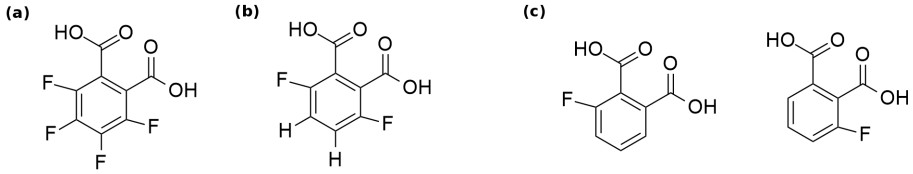

Figure 2.2: O-pthalic acid linkers present in (a) TKL-107, (b) TKL-106 and (c) TKL-105. The two possible structures in case of TKL-105 are shown leading to a site disorder.

structurally similar to TKL-106 except that it has only of the two equivalent positions substituted leading to 2 possible structures because of site disorder as shown in Figure 2.2. Herein, we have considered one of the structures using which we generalize the arguments to the other structure. Further description of the system and methods used is given in the subsequent section.

2.2 Computational Details

Both classical and ab initio methods are employed here to understand CO_2 uptake in this series of MOFs.

Classical molecular dynamics (MD) simulations are carried out in the canonical ensemble (constant NVT) to study diffusion of CO_2 inside the MOFs and for preliminary identification of adsorption sites. Partial charges and Lennard-Jones (LJ) parameters for CO_2 are taken from the TraPPE force field.[2] LJ parameters for the MOFs are taken from the Universal force field (UFF).[3] Partial charges for atoms of the MOF are calculated using the 'Density derived electrostatic charges' (DDEC) method[4] from the valence electron densities and these are used to model electrostatic interaction between the MOF and adsorbed CO_2 for evaluation of binding sites. Cross terms are obtained using Lorentz-Berthelot combination rules. Temperature of the system is maintained using Nosé-Hoover thermostat.[5] All classical simulations were performed after removal of solvent.

12-6 LJ functional[6] is used to calculate pairwise interactions in direct space within a

cutoff distance of 12.8 Å. Beyond this distance, long-range electrostatic interactions are calculated in reciprocal space using particle-particle particle-mesh method with an accuracy of 1 part in 10^5.[7] The MOF is kept frozen in all the simulations which obviates the need to develop intramolecular parameters for the MOF.

For the calculation of time correlation functions, a supercell of size 2 X 2 X 2 of the experimental unit cell was used was used with appropriate number of CO_2 molecules inserted using a Grand Canonical Monte Carlo (GCMC) code developed in-house.[8] All the atoms of the MOF are considered to be charge neutral. The simulations are run at 273 K for 30 ns with a timestep of 2 fs.

For identification of binding sites and calculation of heats of adsorption, the experimental unit cell is used with charges derived from DDEC. The simulation is performed at 20 K so that a randomly inserted CO_2 molecule moves slowly and samples the entire space within the MOF. Binding sites are identified by looking at the potential energy of the system with time and subsequent energy minimizations. A timestep of 1 fs is used in these simulations. Simulations were run for about 2 ns with different starting position of CO_2. All MD simulations are done using the LAMMPS code.[9] Corresponding analysis codes are self-written in FORTRAN 90.

Ab initio calculations are carried out for a deeper understanding of binding sites and to elucidate interactions present between CO_2 and linkers of the MOF.

To find the positions of CO_2 molecules inside the respective frameworks, periodic density functional theory (DFT) calculations were carried out using the QUICKSTEP module in the CP2K software.[10] Valence electrons were treated in a mixed basis set with a plane wave energy cut-off equal to 280 Ry. The short-range version of the double- single polarization basis set was used. The effect of core electrons and nuclei was considered by using the norm-conserving pseudo-potentials of Goedecker-Teter-Hutter (GTH).[11] The exchange and correlation interactions between electrons were treated with the Perdew-Burke-Ernzerhof (PBE) functional.[12] van der Waals

interactions between the gas and the framework are very important and, therefore, their effects were accounted for by employing empirical corrections prescribed by Grimme.[13] We used the DFT-D3 scheme to calculate the cell volume in each of the cases. The optimized cell parameters are presented in the next section. Calculations using the PBE functional along with D3 van der Waals corrections reproduced the experimental cell parameters within acceptable error limits. Geometry optimization was carried out with an appropriate number of CO_2 molecules introduced into the formula unit of the MOF. The binding energy between gas molecules and linkers of the MOF was calculated in the following manner:

$$\Delta E = E_{mof+gas} \text{ - } \mathrm{E}_{mof} \text{ - } \mathrm{E}_{gas}$$

where $\mathrm{E}_{mof+gas}$ is the energy of the MOF with one molecule of CO_2, E_{mof} is the energy of the MOF and E_{gas} is the energy of the isolated gas molecule calculated in the same simulation cell as the MOF. During geometry optimization, component of forces on every atom was less than 10^{-4} a.u. Basis superposition errors (BSSE) in the energy are corrected using the counterpoise method.[14]

Born-Oppenheimer molecular dynamics calculations are also carried out using QUICKSTEP module[10] which uses a mixed basis set in which Kohn-Sham orbitals[15,16] are expanded in a Gaussian type atom-centered basis set while the electron density is represented using auxiliary plane wave basis set. All other details being the same as above, these simulations are run at 273 K and 50 K with a timestep of 0.5 fs in both cases. Nosé-Hoover thermostat[5] is used to control the temperature of the system. For all ab initio calculations, the experimental unit cell is used with solvent molecules removed. Once again, analysis codes have been written in FORTRAN 90.

All structure visualisation was carried out using VMD,[17] Gaussview[18] and Mercury.[19]

2.3 Results and Discussions

2.3.1 Cell parameter optimization

The experimentally determined crystal structures of the three MOFs reveal three molecules of water present per monoclinic unit cell in each case.[1] However, the experimental studies on CO_2 adsorption were carried out with dehydrated MOFs and therefore, we removed the water molecules from the experimental unit cell prior to the optimization of cell parameters through DFT-based methods. Symmetry present in the unit cell is maintained in the cell parameter optimization with γ being relaxed. We find excellent agreement in cell volumes between the experimental data for the as-synthesized compound and computed data for the desolvated MOF as summarized in Tables 2.1-2.3 and, therefore, the experimentally obtained cell parameters are used without modification in simulations. As expected from experimental observations, the volume difference is least in TKL-107 and maximum in TKL-105 suggesting stability of the crystal structure associated with fluorination.

Table 2.1: Optimization of cell parameters in TKL-107

Method	a (Å)	b (Å)	c (Å)	α°	β°	γ°	V (Å)^3)
Experiment	15.1738	15.1738	18.859	90.00	90.00	120.00	3760.479
DFT	15.154	15.154	18.769	90.00	90.00	119.80	3740.129

Table 2.2: Optimization of cell parameters in TKL-106

Method	a (Å)	b (Å)	c (Å)	α°	β°	γ°	V (Å)^3)
Experiment	15.540	15.540	18.679	90.00	90.00	120.00	3906.500
DFT	15.480	15.480	18.539	90.00	90.00	119.70	3858.902

Table 2.3: Optimization of cell parameters in TKL-105

Method	a (Å)	b (Å)	c (Å)	α°	β°	γ°	V (Å)^3)
Experiment	15.698	15.698	18.557	90.00	90.00	120.00	3960.300
DFT	15.618	15.618	18.337	90.00	90.00	119.80	3897.557

It is interesting to note that such excellent agreements in cell volume are obtained in each case despite removing the solvent from the MOF while significant deviation is observed when the solvated MOF is optimized as shown in Figure 2.3.

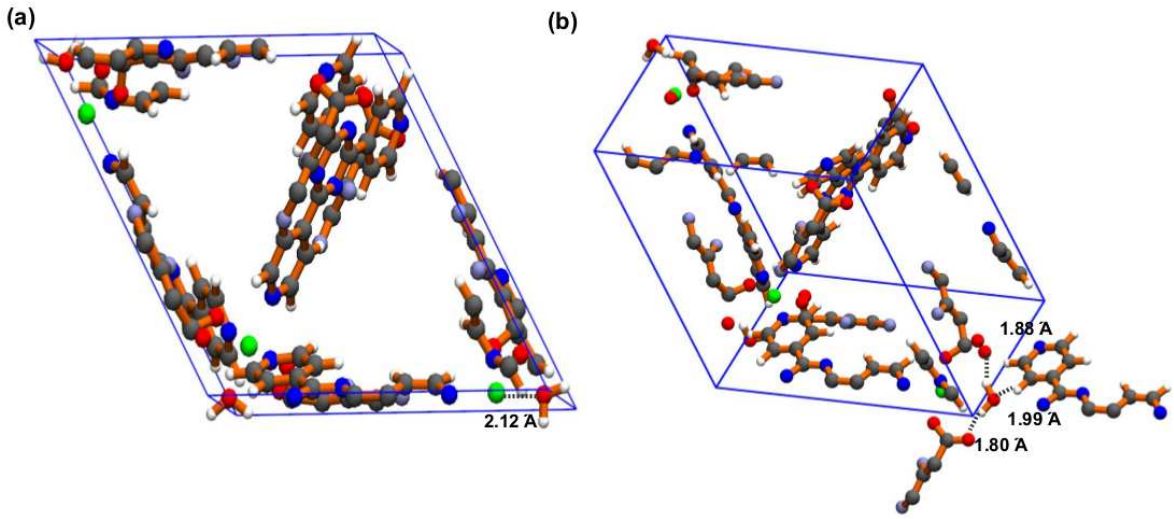

Figure 2.3: (a) Experimentally determined structure of TKL-107 showing possible Lewis acid-base interactions. (b) Geometry optimized structure of TKL-107 within PBE/D3 level of theory showing water molecules oriented away from Ni(II) ions. Possible favourable interactions are indicated with relevant distances. Color codes for MOF atoms: grey - C, blue - N, white - H, Green - Ni, ice blue -F, red -O.

Adsorption sites in MOFs are often identified based on the positions initially occupied by solvent molecules. Therefore, the hydrated structure of TKL-107 was optimized to predict the possible effects of desolvation and we observe that the water molecules bend outwards away from the metal site to facilitate favourable hydrogen bonding interactions with surrounding atoms as indicated in Figure 2.3b. Therefore, it seems probable that the removal of solvent does not really produce a binding site near the metal atom and and indeed, we also observe from geometry optimizations that *the CO_2 molecule does not bind at the open metal site initially occupied by water as per the experimental structure.* Strong similarity in structure makes this arguments valid for all three MOFs in consideration. Nonetheless, all further simulations have been carried out after removal of water from experimentally obtained structures.

2.3.2 Diffusion of CO_2 in TKL MOFs

As described earlier, constant NVT simulations are performed with appropriately large supercells and time correlation functions are evaluated from trajectories of CO_2 molecules thus obtained. As mentioned earlier, the MOFs are kept rigid during these simulations. TKL-107 shows an exceptional CO_2 uptake of 150 cm^3/g at 1000 torr and 273 K and, therefore, diffusion coefficients are calculated at a CO_2 loading characteristic of this temperature and pressure in all three MOFs. The appropriate number of CO_2 molecules calculated from experimentally obtained isotherms are inserted into the desolvated supercell. Initial coordinates of CO_2 molecules are generated using the GCMC technique and the positions of the CO_2 molecules are written out every 4 ps for 30 ns. This trajectory is utilized to calculate mean-square displacements (MSDs) of CO_2 molecules. Further, in case of TKL-107, velocities of CO_2 molecules are written out every 2 fs for a duration of 5 ps to evaluate their velocity autocorrelation function (VACF).

MSD of atoms in a simulation can easily be calculated from the generated trajectories.

$$< r^2(t) >=<\mid \vec{r}(t) - \vec{r}(0) \mid^2> \tag{2.1}$$

The displacements thus obtained from the trajectory are averaged over all atoms as a function of time. Care must be taken to avoid the use of periodic boundary conditions while analyzing the trajectories of atoms in the simulation. The self-diffusion coefficient D is evaluated from the MSD using Einsteins relation by fitting the MSD plots to straight lines as shown in Figure 2.4b. Equation 2 demonstrates how D is obtained from the respective MSDs.

$$D = \lim_{t\to\infty} \frac{1}{6t} <\mid \vec{r}(t) - \vec{r}(0) \mid^2> \tag{2.2}$$

VACF defined in Equation 3 is evaluated for CO_2 molecules in TKL-107 from the velocities written out at every time step. It is an important time correlation function as it reveals the underlying nature of the dynamical processes operating in a molecular system. It is evaluated for CO_2 in TKL-107 using velocities written out at every time step. It decays sharply to zero within small timescales and, therefore, is evaluated only for a duration of 5 ps. VACF can be used to evaluate diffusion coefficients and this is done for CO_2 in TKL-107. A part of the VACF is shown in Figure 2.4c.

$$< \vec{v}(0).\vec{v}(t) >= \frac{1}{N}\sum_{i=1}^{n} \vec{v}_i(0).\vec{v}_i(t) \tag{2.3}$$

Provided that the VACF decays to zero at long time, the function may be integrated numerically to calculate D. This is a special case of a more general relationship between the VACF and the mean square displacement, and belongs to a class of formulae known as the Green-Kubo relations, which relate correlation functions to the so-called transport coefficients. It should be verified that the running integral converges for the timescale used before attempting to make use of the relation.

$$D = \frac{1}{3}\int_{t=0}^{\infty} < \vec{v}_i(0).\vec{v}_i(t) > dt \tag{2.4}$$

The self-diffusion coefficient for CO_2 is found to be 8.56 X 10^{-9} m^2/s in TKL-107, 11.114 X 10^{-9} m^2/s in TKL-106 and 11.882 X 10^{-9} m^2/s in TKL-105. It is verified for TKL-107 that the Green-Kubo relation gives nearly the same self-diffusion coefficient as obtained from the MSD. These values agree well with diffusion coefficients of CO_2 typically seen in literature for fluorinated MOFs. The trend in D observed is understandable because TKL-107 is perfluorinated with a smaller pore volume and, therefore, the diffusion coefficient of CO_2 is least in TKL-107.

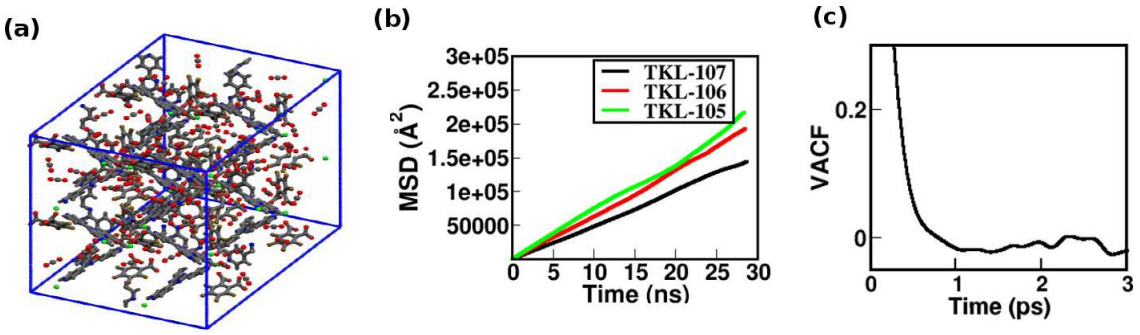

Figure 2.4: (a) Snapshot from the trajectory showing 98 CO_2 molecules in the supercell of TKL-107. (b) MSDs plotted as a function of time for each of the three MOFs. (c) VCF for CO_2 molecules in TKL-107 plotted as a function of time.

2.3.3 Binding sites

Adsorption sites were identified using both classical molecular dynamics simulations and DFT-based geometry optimizations. Calculations based on DFT were mainly used to obtain an insight into the interaction between the gas molecule and the organic linkers present in the MOF. The three MOFs in consideration here have largely similar structures with varying fluorine functionalization only on the o-phthalic acid linker and, therefore, have very similar pore architectures and functionalization as shown in Figure 2.5. Pore architectures are almost identical in TKL-106 and TKL-105 except that only one of the equivalent positions on the o-phthalic acid linker is fluorinated and so, pore architectures only in TKL-107 and TKL-106 are depicted using the van der Waals representation. Consequently, most adsorption sites are common in all three MOFs and these shall be highlighted with emphasis on how the chemical environment tunes interaction with the adsorbed CO_2 molecules and corresponding enthalpies of adsorption.

The specific nature of the interactions between the adsorbed CO_2 and the corresponding frameworks can be best understood by looking at electron density differences within the region of interest. In general, two types of interactions are possible with an adsorbed CO_2 molecule based on the linkers present in the systems of interest: (i) π-π interactions between the aromatic rings and electron cloud of CO_2 and (ii) Lewis

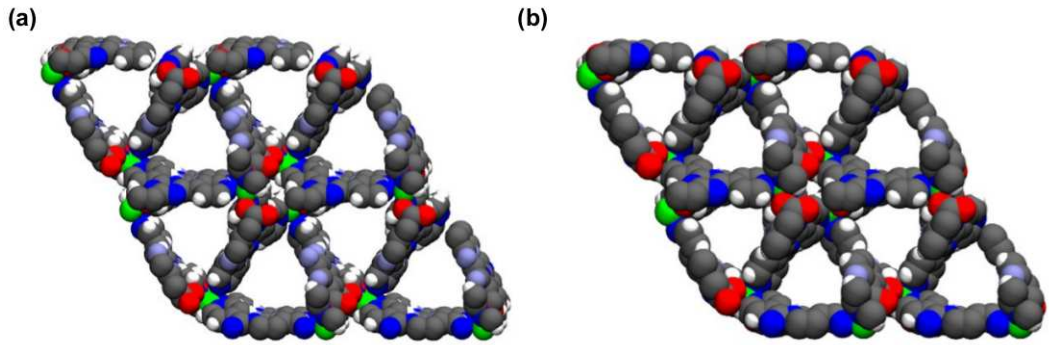

Figure 2.5: Van der Waals representation of pore architecture and chemical environments viewed along the c axis in (a) TKL-107 and (b) TKL-106. Color codes for MOF atoms: grey - C, blue - N, white - H, Green - Ni, ice blue - F, red -O.

acid-base interactions between the electron deficient C of CO_2 and Lewis basic sites in the MOF such as F atoms or O atoms of the carboxylate groups. In principle, there are several binding sites possible with either or both of the above-mentioned interactions leading to a large number of adsorption sites and binding energies. Figure 2.6 highlights organization of possible binding sites in TKL-107. In particular, we show distances between relevant F groups on the o-phthalic acid ligand and O atoms of the carboxylate group to indicate that they are relatively close to each other. It is important to note that the O atoms spoken of here are towards the edge of the unit cell and, therefore, we show one such o-phthalic acid group by replicating atoms into the subsequent unit cell. For the sake of convenience, only the O atoms of the carboxylate group at the boundary of the unit cell are shown in most figures. Binding sites in TKL-107 are exhaustively listed out and discussed following which we try to generalize these arguments to the other two MOFs in consideration.

Binding sites in TKL-107

Preliminary identification of binding sites for CO_2 in TKL-107 is obtained through classical MD simulations at sufficiently low temperatures to allow the inserted molecules to sample the complete pore environment within the MOF. The resulting configurations are then optimized using DFT-based methods and, subsequently,

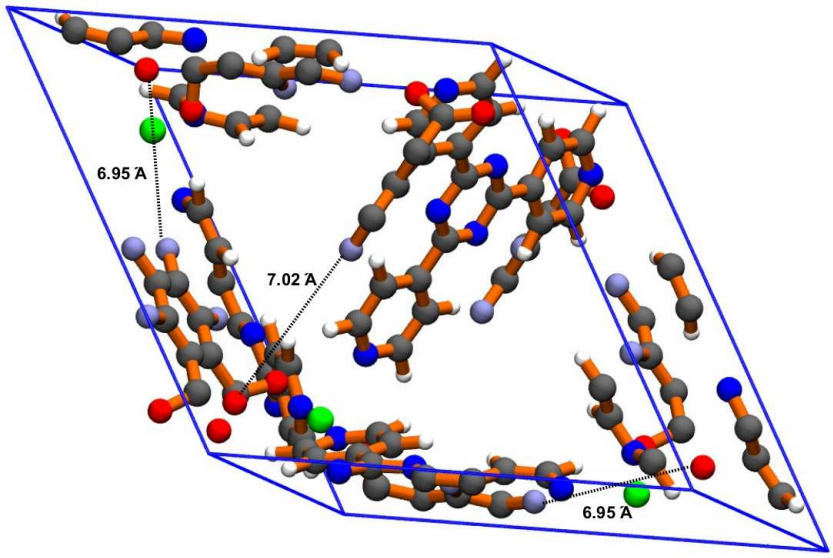

Figure 2.6: Pore functionalities and chemical environment in TKL-107. The distances between corresponding fluorine groups and oxygen atoms of the carboxylate groups are indicated here to illustrate the topology of the MOF. Color codes for MOF atoms: grey - C, blue - N, white - H, Green - Ni, ice blue - F, red -O.

ab initio MD simulations were carried out both at 273 K and 50 K to explore the regions of interest. Among the various binding sites shown in Figure 2.7a to understand the trends in isosteric heat, two distinct energetically favourable binding sites are identified: (i) the carboxylate groups on the o-phthalic acid ligands and (ii) F groups in the vicinity of aromatic rings. Binding sites within these regions are explored through different ab initio MD simulations at 273 K and 50 K and these are detailed later. These sites correspond to highest binding energies and are shown in Figure 2.7a as g, a and e respectively. However, the experimentally obtained zero coverage isosteric heat shown in Figure 2.7b calculated at 273 and 298 K is much lower and shows a gradual increase with higher gas uptake. Therefore, it seems probable that the topology of TKL-107 is such that CO_2 does not bind at the carboxylate site. In particular, it is interesting to note the environment around the carboxylate group in TKL-107. As mentioned earlier, F atoms at the the 4 position on the o-phthalic acid ring and the indicated carboxylate groups shown in Figure 2.6 are reasonably close to each other and, therefore, behaviour of the adsorbed CO_2

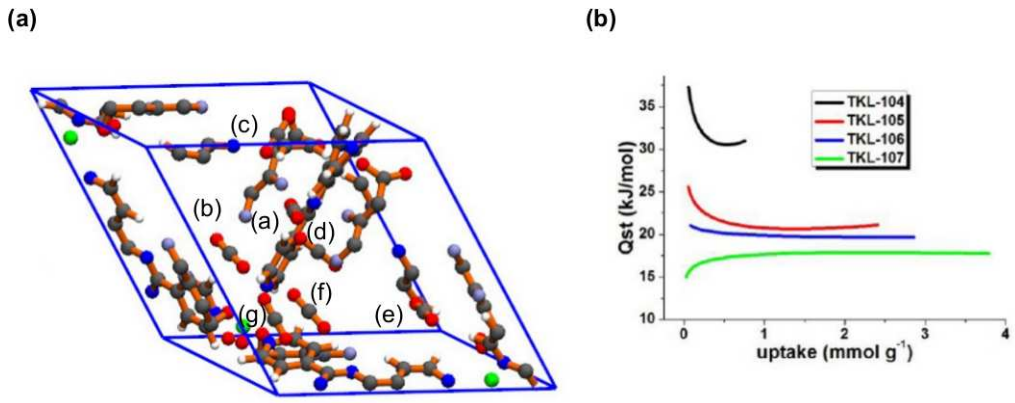

Figure 2.7: (a) Possible adsorption sites for CO_2 in TKL-107. (b) Experimental isosteric heats for various FMOFs in the TKL series.[1] Color codes for MOF atoms: grey - C, blue - N, white - H, Green - Ni, ice blue - F, red -O while carbon and oxygen in CO_2 are shown in grey and red respectively.

in this region should have significant effects on binding sites and energies.

The binding sites mentioned are found through classical MD simulations and further verified by geometry optimizations. Other possible binding sites in TKL-107 are found using a combination of chemical intuition and geometry optimizations in order to achieve experimentally obtained values and understand increase in isosteric heat with CO_2 uptake. Thus, an array of possible sites and binding energies are obtained. Various adsorption sites are labelled and interactions in each case are understood from electron density differences. Theoretically calculated binding energy for CO_2 bound at g and corresponding interactions with linkers are very similar across the three MOFs with minor variations. Moreover, this value of about 26 kJ/mol obtained from calculations is experimentally realized in TKL-105 for reasons we investigate later. Therefore, site g is discussed with regard to TKL-106 and 105 and is left out here. Here, the focus is on other binding sites to understand the experimental trends in isosteric heat with coverage. Binding energies for CO_2 in TKL-107 calculated through classical MD are compared in Table 2.4 with those obtained from DFT for various binding sites.

It is found that binding energies obtained through DFT are in better agreement with

Table 2.4: Binding sites and energies for CO_2 in TKL-107

Binding site	DFT (kJ/mol)	Classical MD (kJ/mol)
(a)	-21.63	-28.13
(b)	-16.23	-20.37
(c)	-15.55	-20.36
(d)	-19.84	-21.92
(e)	-21.77	-25.58
(f)	-18.39	-24.75

experimental trends. Binding energies for each of the sites are overestimated in the classical simulations as seen from Table 2.4, but the trends are consistent. Indeed, a and e shown in Figure 2.7a are easily obtained through classical MD simulations because there exist sharp minima in the energies in these regions. These sites are very similar in terms of chemical environment. It is verified later through ab initio MD simulations within significant regions of interest that the sites g and a arrived at correspond to local minima. From Table 2.4, c is the site with lowest binding energy and is mentioned here only to possibly account for the zero coverage heat experimentally observed in TKL-107. All the other sites have reasonable energies to account for the enthalpies obtained at higher loading except for g which corresponds to a much higher energy than that observed experimentally even at a higher uptake. With the exception of f because of differences in the extent of fluorination, all other binding sites are possible in all three MOFs. However, they have been exhaustively detailed only for TKL-107 as energies obtained here for each of the sites are nearly reproducible in the other MOFs in consideration as well. In fact, we believe the absence of binding site f is key in determining the behaviour of CO_2 around the carboxylate site in TKL-105. TKL-106 has an additional F atom attached at the 3 position on the o-phthalic acid ring which may result in anomalous properties.

From electron density differences, we understand various interactions possible between CO_2 and the linkers of the MOF in TKL-107 and these are shown in Figure 2.8. As mentioned earlier, π-π interactions and Lewis acid-base interactions are seen

in a,e and d. Only Lewis acid-base interactions are seen in f and only π-π interactions are seen in b and c. The binding energies obtained can easily be justified based on the interactions observed. We proceed to comment on binding sites and energies in TKL-106 and TKL-105 using an idea of binding sites obtained in TKL-107.

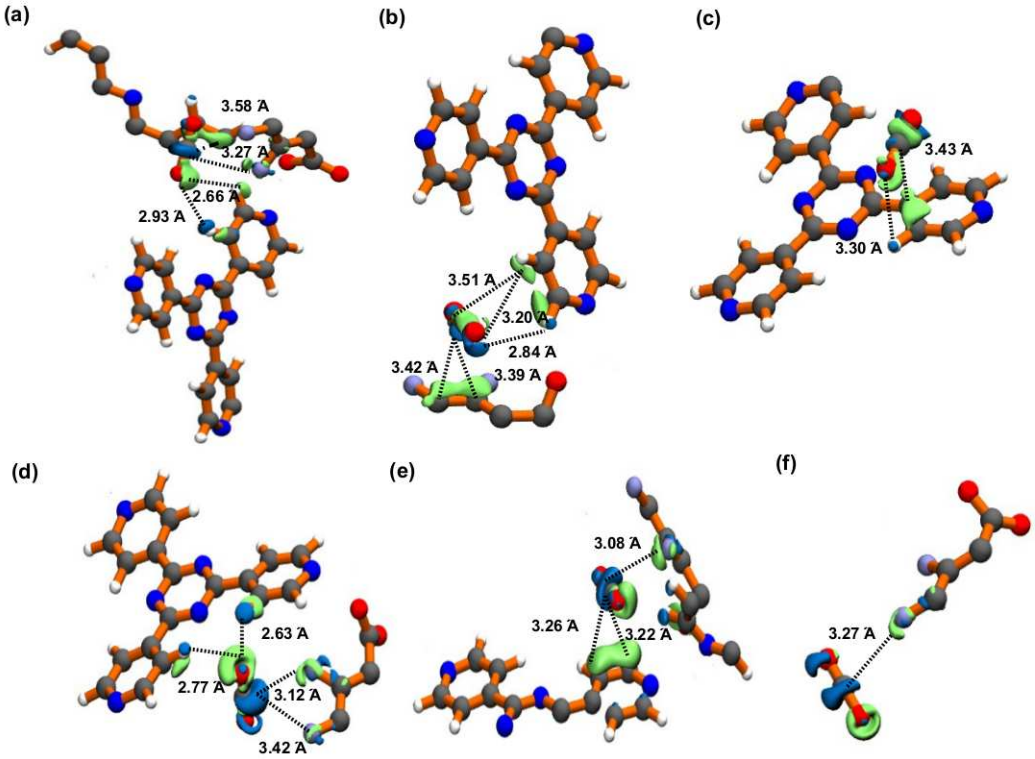

Figure 2.8: CO_2 interacting with linkers of TKL-107 at various binding sites as indicated in Figure 2.7a. Cyan and lime regions indicate decreased and increased electron densities, respectively, with respect to the isolated MOF and the isolated gas molecule. Isosurface value is 4 X 10^{-4} a.u. Color codes for MOF atoms: grey - C, blue - N, white - H, Green - Ni, ice blue - F, red -O while carbon and oxygen in CO_2 are shown in grey and red respectively.

Binding sites in TKL-106 and TKL-105

Binding energies for CO_2 adsorption in TKL-106 and TKL-105 are calculated using DFT calculations alone mainly because the values are very similar to those obtained for TKL-107. For TKL-106 and TKL-105, all the binding sites are not listed out. Only the ones energetically feasible are listed. For TKL-105, this corresponds only

to the carboxylate binding site, g and the energies obtained are compared with experiment. For TKL-106, we list out sites corresponding to locations of sites a, e and g in TKL-107. Similar binding sites are denoted as in TKL-107 for clarity and consistency.

Table 2.5: Binding sites and energies for CO_2 in TKL-106

Binding site	DFT (kJ/mol)
(e)	-21.45
(a)	-22.39
(g)	-25.08

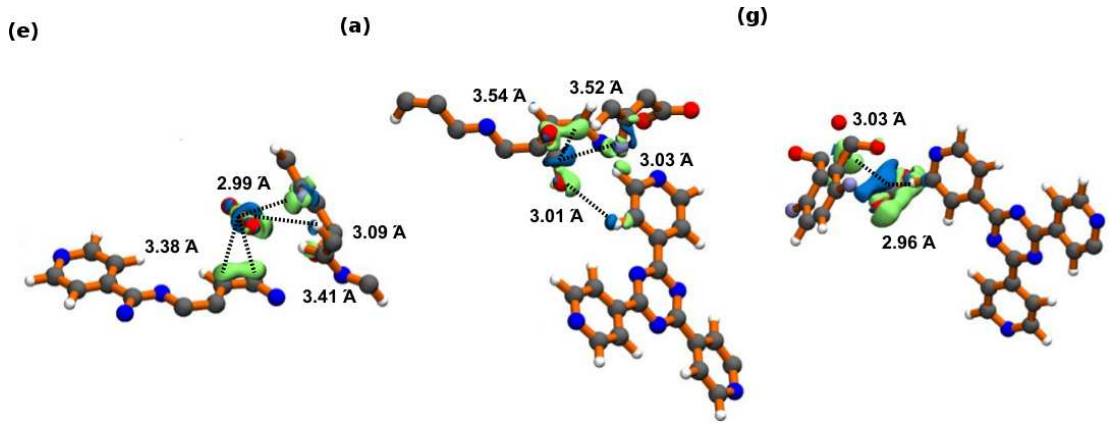

Figure 2.9: CO_2 interacting with linkers of TKL-106 at various binding sites denoted as in Figure 2.7a. Cyan and lime regions indicate decreased and increased electron densities, respectively, with respect to the isolated MOF and the isolated gas molecule. Isosurface value is 4 X 10^{-4} a.u. Color codes for MOF atoms: grey - C, blue - N, white - H, green - Ni, ice blue - F, red -O while carbon and oxygen in CO_2 are shown in grey and red respectively.

As mentioned earlier, the energies obtained for binding sites a and e are very similar because of identical chemical environments. We see that this trend remains in TKL-106 as well. g corresponds to CO_2 binding at the O of the carboxylate group in TKL-106 as indicated earlier. Adsorption at this site gives almost identical theoretical values in all three MOFs and agrees very well with experiment in the case of TKL-105 with a binding energy of around 26 kJ/mol. Therefore, we do not report binding energies for TKL-105 separately because the carboxylate site seems to be the binding

site and the values are very similar to those mentioned for g in TKL-106. Electron density differences for binding sites in TKL-106 shown in Figure 2.9 reveal similar interactions as in TKL-107 and an extremely strong Lewis acid-base interaction for binding in the vicinity of the carboxylate group which was not discussed for TKL-107.

2.3.4 Ab initio molecular dynamics simulations

As discussed previously, we try to understand trends in enthalpies of CO_2 adsorption by examining ab initio MD simulations performed within regions of interest. Trajectories around binding sites are mainly considered here for analysis and the colour code for the MOF atoms in all trajectories is kept the same as before. Therefore, the same is not mentioned in every figure.

Ab initio MD simulations of CO_2 in TKL-107 around binding sites g and e

Ab initio MD simulations are performed initially with the MOF held rigid at 273 K to find the most energetically favourable binding sites within a particular region. This not only gives us an understanding of the region within the MOF energetically but also helps us verify the binding sites obtained through optimization. In Figure 2.10, we consider trajectories of CO_2 around binding sites g and e in TKL-107. Relatively short simulations of 1 ps are performed as we are interested in the movement of the gas molecule within the vicinity of the relevant functional groups. Binding energies are plotted against time for each of these trajectories and the most energetically favourable positions of CO_2 are found to agree with those obtained from optimizations. The trajectory around g suggests that the binding site with the greatest enthalpy of adsorption in the region of the carboxylate group is similar to that obtained in TKL-106 and TKL-105. Indeed, the CO_2 molecule moves towards

the O of the carboxylate group indicated in the unit cell as seen in Figure 2.10a. This is understandable as it is the most energetically favourable site in all MOFs in consideration here.

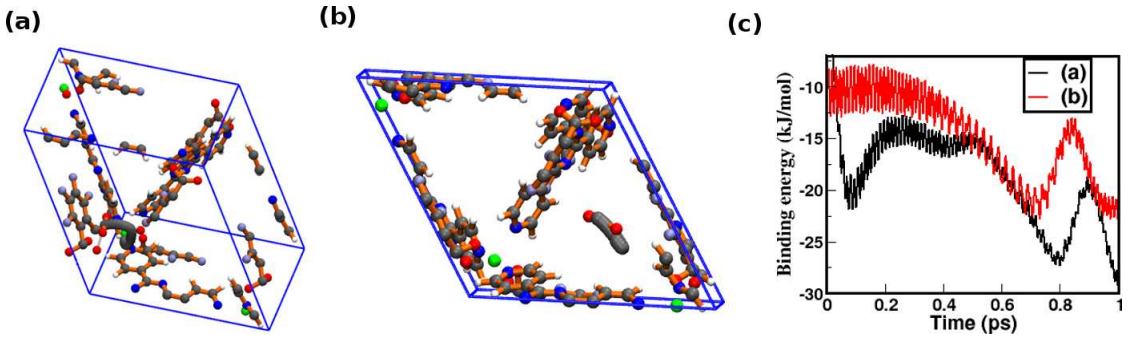

Figure 2.10: (a) Trajectory of CO_2 in TKL-107 around g at 273 K with MOF fixed. (b) Trajectory of CO_2 in TKL-107 around binding site e at 273 K with MOF fixed. (c) Binding energy for each trajectory plotted with time.

Ab initio MD simulations of CO_2 around g in TKL-107: relaxed MOF

As discussed earlier, the region around g is interesting in terms of CO_2 behaviour and, therefore, ab initio MD is carried out with atoms of the MOF relaxed at two different temperatures. Figures 2.11a and 2.11b exhibit results of simulations with the same initial position of CO_2 as in Figure 2.10a but with the MOF relaxed to understand how CO_2 interacts in a region flanked by two functionalities close to each other when the MOF is free to move. We carry out simulations at 273 K and 50 K respectively and we notice significant differences in trajectories in the 1 ps run. The simulation at 50 K shown in Figure 2.11b resembles both classical and ab initio MD simulations performed with the MOF fixed at 273 K in that the CO_2 molecule gradually approaches the carboxylate binding site. However, a strikingly different trajectory, shown in Figure 2.11a, is observed when the MOF is relaxed at 273 K which goes to show that *the MOF undergoes structural changes with temperature and this affects CO_2 binding in this region dramatically.* We believe the complication in TKL-107 arises because of the presence of the fluorine group in the

vicinity and therefore, we look at distances between the C atom of CO_2 and O of the carboxylate group throughout each of the trajectories. We also consider distances between C and the F atom on the o-phthalic acid linker during the course of the simulation to understand how CO_2 interacts within this region of the MOF. The corresponding distances mentioned are plotted in Figure 2.11d and we notice that the CO_2 significantly interacts with the F atom in the trajectory shown in Figure 2.11a as depicted in binding site f in Figure 2.8. Emphasis was laid on this binding site being absent in TKL-106 and TKL-105, for this reason. A simulation is also run deliberately placing the CO_2 closer to the F site and we observe the trajectory in Figure 2.11c and plot the corresponding distances as mentioned.

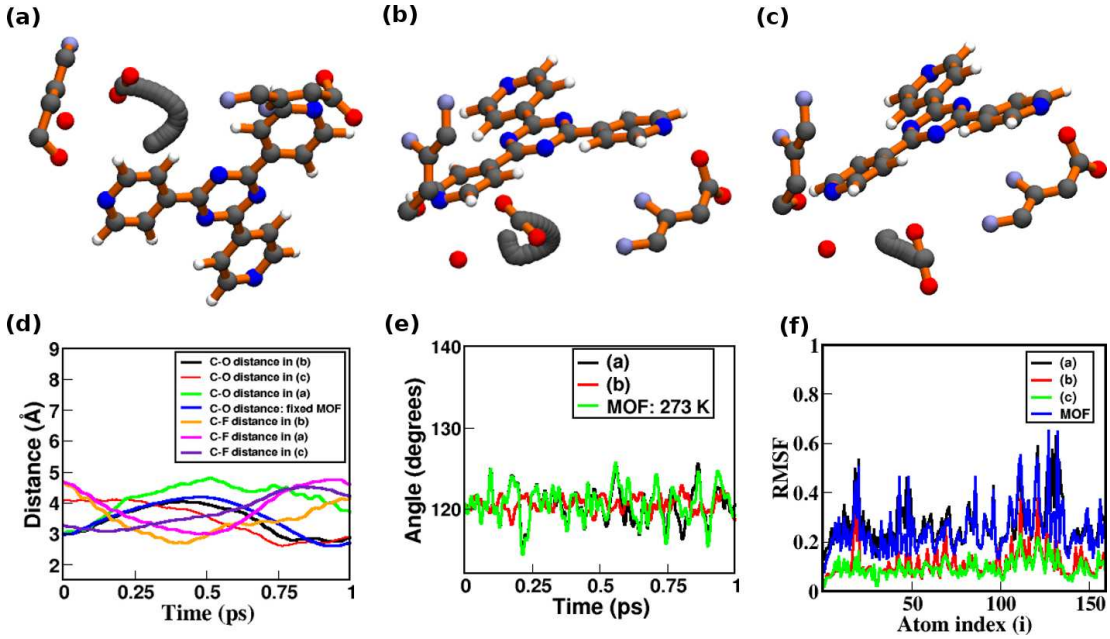

Figure 2.11: (a) Trajectory of CO_2 in TKL-107 around g with MOF relaxed at 273 K. (b) Trajectory of CO_2 in TKL-107 around g with MOF relaxed at 50 K. (c) Trajectory of CO_2 in TKL-107 oscillating about the F site with MOF relaxed at 50 K. (d) Distances between C of CO_2 and the respective functional groups for each of the simulations (a) to (c). (e) Fluctuations in the angle between the pyridine ring closest to the CO_2 molecule and the rest of tpt ring. (f) RMSFs (Å)/fs$^{0.5}$ for atoms of TKL-107 for (a),(b),(c) and the isolated MOF relaxed at 273 K.

To look at particular structural changes in the MOF that might be responsible for this behaviour at a higher temperature, we evaluate the mean square fluctuations

(MSFs) in each atom of the MOF using the trajectory generated from each of these simulations. MSFs are calculated by evaluating average positions of all atoms of the MOF over all time steps:

$$MSF = \frac{1}{T}\sum_{t=1}^{T}(\vec{r}(t) - \vec{r}_{avg})^2 \tag{2.5}$$

where $\vec{r}_{avg}$ is the reference position of the particle which is typically the time-averaged position and T is the time over which one wants to average. We evaluate the square root of the above quantity denoted as RMSF and plot it against atom index, i. It gives an idea of the distortions in the structure of the MOF during the simulations. This is done for the three trajectories considered in Figures 2.11a-c and for the isolated MOF without any CO_2 introduced and these are plotted in Figure 2.11f.

In the trajectory shown in Figure 2.11a at 273 K, distance between C of CO_2 and F on the o-phthalic acid ligand falls well below 3 Å suggesting the presence of a potential well in that region. Further, we notice the distance between CO_2 and the O atom of the carboxylate group in this trajectory increases whereas at 50 K, the distance increases a little at first but then quickly falls off as shown in Figure 2.11b for the same starting geometry; the maximum C-O distance is in fact, lesser than that obtained from a fixed MOF simulation as in Figure 2.10a at 273 K. While it can be argued that the CO_2 molecule may come back to location g for longer simulations at 273 K, there is no doubt that there is a significant difference in the pore environment which brings about important differences in trajectories. Therefore, it is expected that distortions in the linkers of the TKL-107 near this site are crucial. From the MSFs plotted, we see that fluctuations at 50 K are more in Figure 2.11b than in Figure 2.11c which once again suggests structural distortion specific to CO_2 position in the MOF. Further, we also plot MSFs for simulations at 273 K: trajectory shown in Figure 2.11a with CO_2 introduced into TKL-107 and for the pure MOF at this

temperature. These fluctuations are obviously higher, but the interesting thing to note is that there are four important fluctuations prominent and present in all MSF plots. These are fluctuations at i values of 18, 20, 111 and 121. These fluctuations are understandably maximum for the trajectory shown in Figure 2.11a. These atom indices elegantly correspond to the four hydrogen atoms on the ring closest to the region of interest as indicated in the unit cell of TKL-107 shown in Figure 2.12a. The corresponding indices and fluctuations can be seen in the MSF plots in Figure 2.11f. This most probably corresponds to the rotation of the ring which is verified by plotting the angle between the terminal ring on the tpt ligand and the rest of the linker in the course of the simulation. The relevant angle is indicated in Figure 2.12a. Fluctuations in this angle plotted in Figure 2.11e are maximum for the trajectory indicated in Figure 2.11a closely followed by those observed in an isolated MOF and obviously, the least in the trajectory shown in Figure 2.11b where the simulation is performed at a lower temperature.

Geometry optmization of intermediate TKL-107 geometries in trajectory 11a

In order to verify that bending of the heterocyclic ring mentioned above is important in determining enthalpies of binding, we take three intermediate geometries of the TKL-107 obtained in the simulation with atoms of the MOF relaxed shown in Figure 2.11a. Geometry optimization of these intermediate structures clearly indicates the movement of the ring in either direction and, therefore, the significant RMSF of the attached hydrogen atoms shown in Figure 2.12a.

The angle between the pyridine ring and the rest of the tpt linker plotted in Figure 2.12b suggests that the pyridine ring rotates considerably and, therefore, this could be a possible factor in pushing CO_2 molecules to low energy sites. In TKL-105, there is no fluorine group in the vicinity of g and, therefore, simulations at 273 K

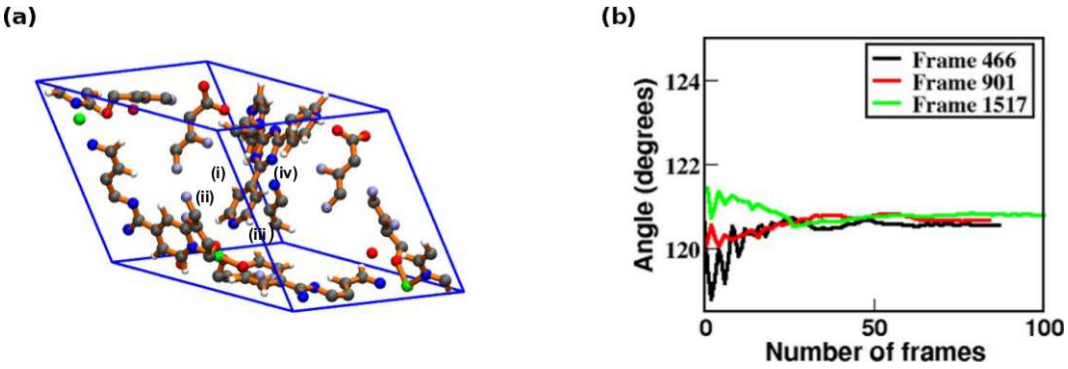

Figure 2.12: (a) Geometry of TKL-107 in frame 901 of the simulation shown in Figure 2.10a. The four H atoms on the pyridine ring with high RMSF values are indicated as well as the angle between the relevant pyridine ring and the rest of the tpt linker. (b) Angle between the pyridine ring and rest of the tpt linker plotted as intermediate geometries of the MOF are optimized within the PBE/D3 level of theory.

produce trajectories that are consistent with intuition and experiment. We verify that this is indeed the case to justify the claim being made.

Ab initio MD simulations of CO_2 around g in TKL-105: relaxed MOF

We repeat the same process for TKL-105 mainly to verify that trajectories around g do not change drastically with temperature. It is also seen that MSFs are not hugely dependent on initial positions of CO_2 suggesting that there are no consistent trends in the distortion of the MOF.

In TKL-105, the MSF values are higher probably because of lower stability of the crystal structure but the absence of a potential well causes the CO_2 molecule to go to g even when the MOF is relaxed at 273 K. Further, trajectories shown in Figures 2.13a and 2.13c are obtained from the same initial position of CO_2 as discussed earlier for TKL-107. Trajectory in Figure 2.13a leads to the favourable binding site as discussed earlier. Trajectory seen in Figure 2.13c is unexpected but it shows that the molecule is not trapped in the region as in TKL-107 and to a slight extent in TKL-106 because of the effect of the F atom on the adjacent position in the ring. Distortions in the angle and MSF values are evaluated as done for TKL-107. There

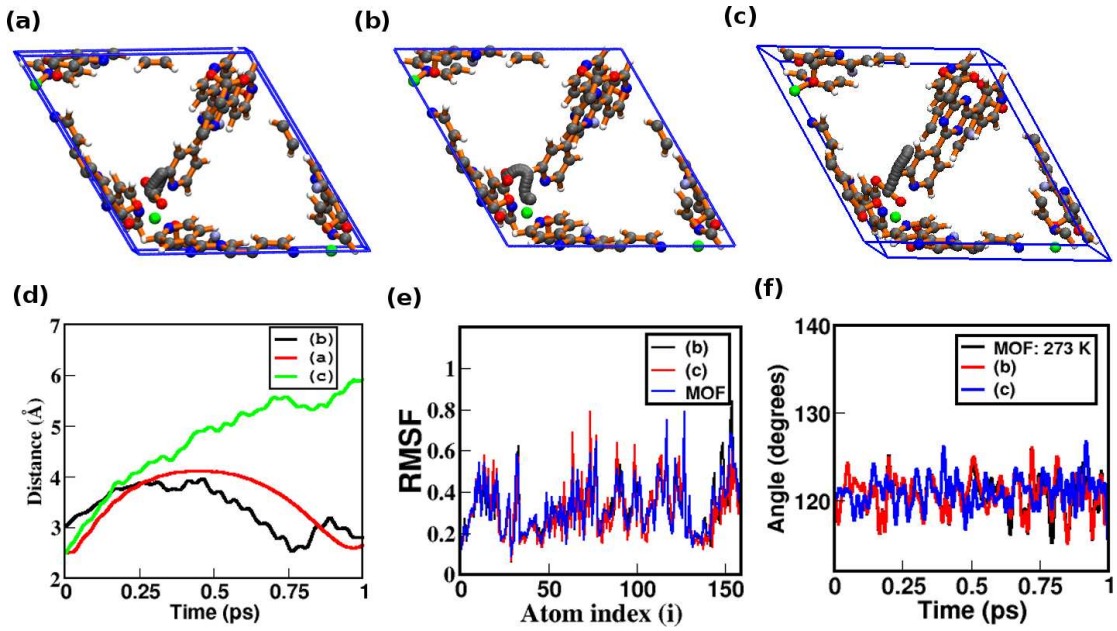

Figure 2.13: (a) Trajectory of CO_2 in TKL-105 around g with MOF fixed at 273 K. (b) Trajectory of CO_2 in TKL-107 around g with MOF relaxed at 273 K. (c) Trajectory of CO_2 in TKL-105 with same geometry as in a with MOF relaxed at 273 K. (d) Distances between C of CO_2 and the respective functional groups for each of the simulations (a) to (c). (e) RMSFs (Å)/$fs^{0.5}$ for atoms of TKL-105 for (b),(c) and the isolated MOF relaxed at 273 K. (f) Fluctuations in the angle between the terminal ring close to the CO_2 ring and rest of the tpt ring.

are no particularly significant trends. RMSF takes highest values for trajectory indicated in Figure 2.13c where the MOF is free to move at 273 K. Fluctuations in the angle between the pyridine ring and rest of the tpt moiety are also higher which indicate lower stability associated with the structure. But unlike TKL-107, there are no characteristic trends which leads us to conclude that the orientation of MOF atoms around CO_2 at the carboxylate site is less important in TKL-105. Trajectories in TKL-106 are similar to those obtained in Figure 2.13a. But the trajectory seen in Figure 2.13c is not obtained and the very obvious explanation for this is the presence of an F group at a position adjacent to the carboxylic acid substituent on o-phthalic acid ring constrains the CO_2 molecule within this region. In TKL-105, one side is unhindered (any one because of the point defect) and we consider this side in the simulation discussed here. Therefore, changes in geometry

of the MOF are critical to understanding binding and an effort was made to gain some insight into this.

2.3.5 Binding energies at higher loading

In a final attempt to understand sequential adsorption and anomalous trends in isosteric heat, binding energy calculations were performed by introducing more than one molecule of CO_2 into the MOFs and from this, an idea of the experimentally obtained binding sites is obtained. In particular, an effort is made to probe co-operativity through DFT calculations. The binding energy for n gas molecules is calculated in the following manner:

$\Delta E = E_{mof+gas}$ - E_{mof} - nE_{gas}

where n is the number of CO_2 molecules inside the MOF. The value of energy thus obtained is then divided by n to yield the average binding energy for comparison with experimental isosteric heat. The motivation behind this is to see how the experimentally obtained curve for isosteric heat can be theoretically accounted for. For TKL-107, the isosteric heat saturates beyond an uptake of 2.5 mmol/g and this corresponds to 3 molecules per unit cell. Therefore, binding energies have been calculated with various combinations of 2 CO_2 molecules inside the MOF and a few combinations involving 3 CO_2 molecules. Binding at the carboxylate site is extensively considered. The energy values obtained are given below. Two of the combinations with CO_2 molecules and all the three molecule combinations considered are shown in Figure 2.14 and the corresponding average energies are calculated and tabulated in Table 2.6.

What is obvious from the above trends is that CO_2 is unlikely to bind at g even after two molecules have been adsorbed in order to be in consistency with experimentally obtained isosteric heats. Each of the above combinations apart from a and b give higher average isosteric heats than can be explained experimentally. Similarly, the

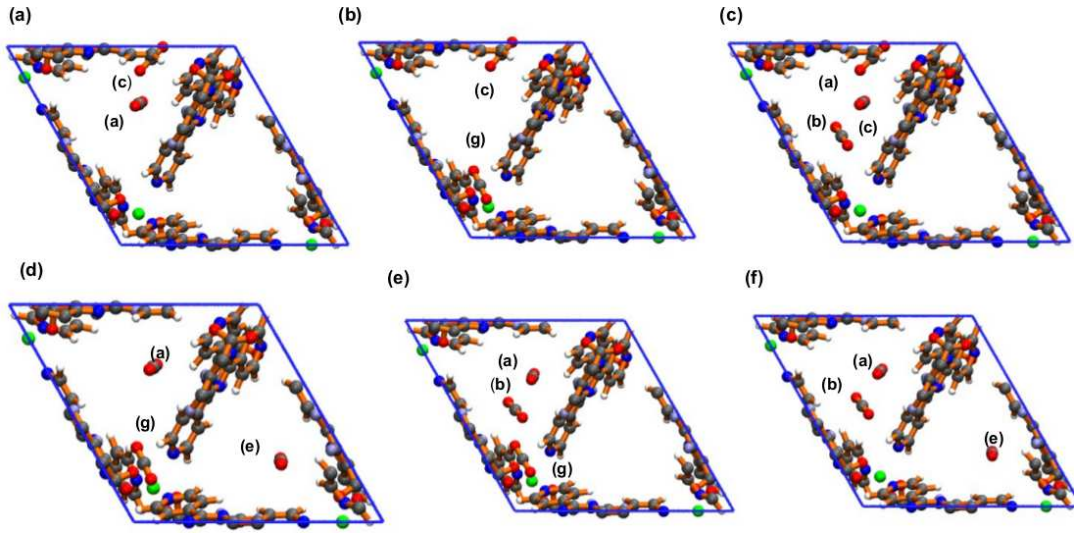

Figure 2.14: Combination of binding sites in TKL-107

Table 2.6: Combination of binding sites and corresponding binding energies in TKL-107

Binding sites	Average binding energies (kJ/mol)
(a), (e)	-21.887
(b), (g)	-21.056
(a), (b)	-18.756
(a), (g)	-24.046
(c), (g)	-20.929
(a), (c)	18.1004
(a), (e), (g)	-23.441
(a), (b), (g)	-20.560
(a), (b), (e)	-18.66
(a), (b), (c)	-17.485

last two entries in Table 2.6 show reasonable agreement with experiment. The possibilities here are far from exhaustive, but an attempt is made to understand sequential binding using DFT. The energies reported everywhere in this work are from 0 K calculations. The calculation of enthalpy at ambient temperatures will involve the addition of an RT term.

2.4 Conclusion

We have tried to model CO_2 adsorption in a class of FMOFs showing unprecedented uptake and explain it in terms of pore architecture and functionalities. Given that predicting trends in gas adsorption with the functionalization of linkers is such a tedious task, these calculations throw light on structure stability associated with fluorination.

The current study also highlights the delicate effects of fluorination on the structure stability and the need to study changes in structure of the framework with temperature. It is particularly interesting to note that low temperatures favour a higher energy binding site, but the MOF shows excellent CO_2 uptake at ambient conditions. The binding sites and energies predicted are in reasonable agreement with experimental data and, therefore, we believe these calculations indeed explain phenomena inherent in the topology of these porous solids.

Classical MD simulations carried out with charges derived from DFT-based methods predict trends in binding energies correctly even though the values are a little higher than experimental values. Trajectories predicted are in good agreement with intuition and experimental observations. Diffusion is a phenomenon that can be understood mainly through MD and, therefore, we have made an attempt to obtain self-diffusion coefficients and these seem to be in agreement with previously published data.

Ab initio calculations carried out helped in the determination of binding sites and trends in isosteric heat that cannot be explained experimentally. It is extremely interesting that minute changes in the linkers of the framework can have such drastic consequences on distortion of the structure with temperature and with the position of the gas molecule. We see that the MOF is not rigid. Linkers are extremely flexible and modulate the pore volume and shape as a function of temperature, thus influencing gas uptake. Kinetic barriers involved significantly influence binding

energy. Therefore, X-ray structures obtained at low temperatures do not convey quite the whole story.

Finally, it is hoped that these efforts to understand gas adsorption in MOFs from a theoretical viewpoint will lead to enhanced efforts in rational theory-guided synthesis.

Bibliography

[1] Zhang, D.-S.; Chang, Z.; Li, Y.-F.; Jiang, Z.-Y.; Xuan, Z.-H.; Zhang, Y.-H.; Li, J.-R.; Chen, Q.; Hu, T.-L.; Bu, X.-H. *Scientific reports 3*, 1–7.

[2] Potoff, J. J.; Siepmann, J. I. *AIChE Journal* **2001**, *47*, 1676–1682.

[3] Rappe, A. K.; Casewit, C. J.; Colwell, K. S.; Goddard, W. A.; Skiff, W. M. *Journal of the American Chemical Society* **1992**, *114*, 10024–10035.

[4] Manz, T. A.; Sholl, D. S. *Journal of Chemical Theory and Computation* **2012**, *8*, 2844–2867.

[5] Hoover, W. G. *Phys. Rev. A* **1985**, *31*, 1695–1697.

[6] Jones, J. E. *Proceedings of the Royal Society of London. Series A* **1924**, *106*, 463–477.

[7] Hockney,; Eastwood, *Computer Simulation Using Particles*; Taylor and Francis, 1988.

[8] Bonakala, S.; Balasubramanian, S. *Submitted* **2015**.

[9] Plimpton, S. *Journal of Computational Physics* **1995**, *117*, 1 – 19.

[10] VandeVondele, J.; Krack, M.; Mohamed, F.; Parrinello, M.; Chassaing, T.; Hutter, J. *Computer Physics Communications* **2005**, *167*, 103 – 128.

[11] Goedecker, S.; Teter, M.; Hutter, J. *Phys. Rev. B* **1996**, *54*, 1703–1710.

[12] Perdew, J. P.; Burke, K.; Ernzerhof, M. *Physical review letters* **1996**, *77*, 3865.

[13] Grimme, S. *Journal of Computational Chemistry* **2006**, *27*, 1787–1799.

[14] Boys, S. F.; Bernardi, F. d. *Molecular Physics* **1970**, *19*, 553–566.

[15] Hohenberg, P.; Kohn, W. *Phys. Rev.* **1964**, *136*, B864–B871.

[16] Kohn, W.; Sham, L. J. *Phys. Rev.* **1965**, *140*, A1133–A1138.

[17] Humphrey, W.; Dalke, A.; Schulten, K. *Journal of Molecular Graphics* **1996**, *14*, 33–38.

[18] Dennington, R.; Keith, T.; Millam, J. *GaussView Version 5*, Semichem Inc. Shawnee Mission KS 2009.

[19] Bruno, I. J.; Cole, J. C.; Edgington, P. R.; Kessler, M.; Macrae, C. F.; McCabe, P.; Pearson, J.; Taylor, R. *Acta Crystallographica Section B: Structural Science* **2002**, *58*, 389–397.

Chapter 3

Theoretical investigations on carbon capture in SIFSIX-Cu MOFs

3.1 Introduction

As discussed in detail in the earlier chapter, porous crystalline solids which exhibit size selectivity and targeted molecular recognition are attractive materials for CO_2 separation and capture. This chapter continues along the same general theme of engineering materials with precise control over pore size and functionality. Here, a series of MOFs with coordinately saturated metal centres and periodically arrayed hexafluorosilicate ($SIF_6{}^{2-}$) ions are considered. This set of Cu MOFs exemplifies crystal engineering aimed at hitting the 'sweet spot' of kinetics and thermodynamics with regard to functionalization and pore architecture. This chapter deals with theoretical calculations aimed at understanding enhancement in carbon capture brought about by minor structural modifications in a family of SIFSIX-Cu MOFs. These modifications are introduced through differences in nitrogenous linkers as shown in

Figure 3.1.

Most importantly, these materials exhibit unprecedented CO_2 adsorption and selectivity over N_2, H_2 and CH_4 , even in the presence of moisture. Therefore, these MOFs are extremely relevant to CO_2 separation in various contexts of carbon capture : pre-combustion (shifted synthesis gas stream, CO_2/H_2), post-combustion (flue gas, CO_2 /N_2) and natural gas upgrading (natural gas clean-up, CO_2/CH_4).

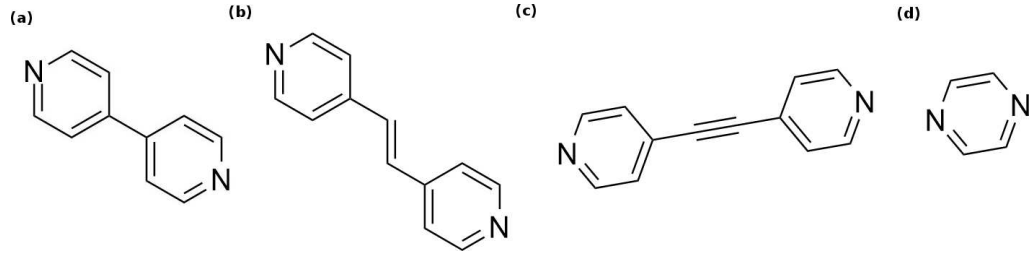

Figure 3.1: Heterocyclic linkers in (a) SIFSIX-1-Cu, (b) SIFSIX-1'-Cu, (c) SIFSIX-2-Cu and (d) SIFSIX-3-Cu.

The four SIFSIX-Cu MOFs considered here are briefly described below. $[Cu(4,4'\text{-bipyridine})_2(SiF_6)]_n$ is a prototypical primitive-cubic net that remains one of the best sorbents for CH_4.[1] It exhibits highly selective CO_2 uptake at 1 bar and 298 K. The uptake of CO_2 shown is commendable for a framework with no open metal sites. This behaviour can be reasonably explained in terms of favourable interactions between CO_2 and the SIFSIX pillars which we try to model here. This framework, denoted as SIFSIX-1-Cu, exhibits one-dimensional square channels with a pore size of 9.54 (Å) aligned by a periodic array of SIFSIX pillars and is prototypical for a family of compounds that lends itself to pore-size tuning. This is considered to be a starting point in this category of MOFs and, therefore, interactions between the adsorbed CO_2 and SIFSIX linkers are modelled here. Further, an effort is made to understand from a theoretical standpoint how structural modifications in this MOF help in enhancing CO_2 capture and uptake. $[Cu(1,2\text{-bis}(4\text{-pyridyl})\text{ethene})_2(SiF_6)]_n$ is an expanded analog of SIFSIX-1-Cu which exhibits larger pores and surface area.[1] It is denoted as SIFSIX-1'-Cu here. CO_2 uptake of SIFSIX-1'-Cu at 1 atm was found

to be 12.1 wt %, around half that of SIFSIX-1-Cu. However, uptake of CO_2 relative to CH_4 remains high at 1 atm even with a surface area twice that of SIFSIX-1-Cu. Isosteric heats (Qst) of adsorption of the two MOFs are comparable with compounds containing open metal sites such as MIL-53 and HKUST-1. Qst values of higher than 40 kJ/mol imply high selectivity for CO_2 but such values can be expected only at low loading if based upon metal binding. Binding energy, binding sites and interactions between CO_2 and linkers of SIFSIX-1'-Cu are investigated here.

Reaction of 4,4'-dipyridylacetylene with $CuSiF_6$ leads to purple rod-shaped crystals of $[Cu(dpa)_2(SiF_6)]_n$, which is referred to as SIFSIX-2-Cu.[2] SIFSIX-2-Cu forms the expected primitive-cubic net with square channels of pore dimensions 13.05 $\AA$. SIFSIX-2-Cu exhibits a CO_2 uptake of 41.4 cubic centimetres per gram at 298 K and 1 bar with a denser polymorph of the same compound showing an uptake of 121.2 centimetres per gram under the same conditions. This is the third compound we consider here.

The isoreticular pyrazine (pyr) based MOF SIFSIX-3-Zn, $[Zn(pyr)_2(SiF_6)]_n$, is also a primitive-cubic net which encloses 3.84 $\AA$ channels.[3] The Qst of CO_2 adsorption for SIFSIX-3-Zn from variable temperature isotherms is around 45 kJ/mol, consistent with the steepness of the CO_2 isotherms. The relatively constant Qst indicates homogeneous binding sites over the full range of loading. These Qst values are in the region favourable for efficient and reversible adsorption. Therefore, the binding is strong but still reversible as verified by modelling studies.[2]

We also consider here the Cu analogue of SIFSIX-3-Zn that shows an even steeper variable temperature adsorption isotherms at very low pressure, indicative of relatively stronger CO_2-SIFSIX-3-Cu interactions.[4] Metal-organic framework crystal chemistry permits the construction of an isostructural MOF based on pyrazine/copper (II) two-dimensional periodic square grids pillared by SIF_6^{2-} anions. Interestingly,

this allows further contraction of the pore to 3.5 $\mathring{A}$ from 3.84 $\mathring{A}$. This enhances energetics of adsorption greatly and consequently, SIFSIX-3-Cu displays CO_2 uptake and selectivity at very low partial pressures crucial in air capture and trace carbon dioxide removal. The adsorption energetics is uniformly distributed and, therefore, the resultant carbon dioxide physical adsorption properties, uptake and selectivity in highly diluted gas streams are largely unachievable with other classes of porous materials. The differences in the various MOFs considered here are summarized in Table 3.1.

Table 3.1: Structural differences in various SIFSIX-Cu-MOFs.

MOF	Unit cell paramaters (Å)	CO_2 uptake (1 bar, 298 K)	ΔH (kJ/mol)
SIFSIX-1-Cu[1]	11.045, 11.045, 8.163	90 cc/g	-27
SIFSIX-1'-Cu[1]	18.847, 18.847, 7.997	50 cc/g	-21
SIFSIX-2-Cu[2]	13.631, 13.631, 7.968	46 cc/g	-22
SIFSIX-3-Cu[4]	6.918, 6.918, 7.9061	56 cc/g	-54
SIFSIX-3-Zn[3]	7.140, 7.140, 7.606	54 cc/g	-45

As expected, the structure of SIFSIX-3-Cu is in very good agreement with the 3D structure of the Zn analogue reported previously,[3] but with a slightly smaller unit cell in terms of volume (378 versus 388 $Å^3$) attributed to the relatively stronger bonding between the Cu(II) and the pyrazine. The smaller unit cell of the Cu analogue leads to enhanced interactions with CO_2 which in turn gives rise to a higher enthalpy of adsorption and a very steep sorption isotherm.

This is one of the first reported efforts on tuning the pore size of physisorption based MOFs to target trace CO_2 removal. The reasoned choice of an appropriate MOF platform characterized by suitable pore size is combined with optimal CO_2 energetics that is strong, uniform and relatively low to facilitate easy desorption.

This is believed to be characteristic of made-to-order porous materials for specific CO_2 capture applications.

The calculations performed here are similar, both in method and motivation, to those in the previous chapter. The focus of the work presented here is to understand CO_2 adsorption in SIFSIX-3-Cu. We try to understand from a theoretical standpoint the important structural differences between SIFSIX-3-Zn and SIFSIX-3-Cu that lead to enhanced adsorption in the latter. CO_2 adsorption in SIFSIX-3-Cu and its associated energetics is understood through molecular simulations in this work.

In the following, the likely binding sites are easily identified on the basis of functionalities present. We then proceed to use ab initio methods to explore regions near functional groups and calculate corresponding binding energies. The dominant interaction in all MOFs studied here is Lewis acid-base interactions between the F atoms in SIF_6^{2-} and C of CO_2. The MOFs in consideration have similar linkers but different architecture. Pore functionalization and architecture is strikingly different in SIFSIX-3-Cu. In particular, an effort is made to understand interactions responsible for experimentally observed trends in binding energies. This understanding is central to effective ligand functionalization and here, we attempt to address these points.

The experimentally obtained desolvated structures are used as a starting point in these calculations. The central focus of this work is SIFSIX-3-Cu and, therefore, we also model CO_2 adsorption in this MOF using classical methods. Further description of the system and methods used is given in the subsequent sections.

3.2 Computational Details

Calculations reported here for SIFSIX-3-Cu are done using both classical and ab initio methods. The other MOFs are investigated using only ab initio methods.

Classical molecular dynamics (MD) simulations are carried out in the canonical ensemble (constant NVT) prior to energy minimization for preliminary identification and verification of adsorption sites in SIFSIX-3-Cu. Partial charges and Lennard-Jones (LJ) parameters for CO_2 are taken from the TraPPE force field.[5] LJ parameters for the MOFs are taken from the Universal force field (UFF).[6] Partial charges are calculated using the 'Density derived electrostatic charges' (DDEC) method[7] from the valence electron densities and these are used to model electrostatic interaction between the MOF and adsorbed CO_2 for evaluation of binding sites. Cross terms are calculated using the Lorentz-Berthelot mixing rules. Temperature of the system is maintained using Nosé-Hoover thermostat.[8]

12-6 LJ functional[9] is used to calculate pairwise interactions in direct space within a cutoff distance of 12.8 Å. Above this distance, long-range electrostatic interactions are calculated in reciprocal space using particle-particle particle-mesh method with an accuracy of 1 part in 10^5.[10] The MOF is kept frozen in all the simulations which obviates the need to develop intramolecular parameters for the MOF.

For identification of binding sites and calculation of heats of adsorption for CO_2 binding in SIFSIX-3-Cu, the corresponding supercell of size 2 X 2 X 2 of the experimental unit cell is used with charges derived from DDEC. The simulation is performed at 20 K so that a randomly inserted CO_2 molecule moves slowly and samples the entire space within the MOF. Binding sites are identified by examining the potential energy of the system with time. Binding energies are estimated by energy minimization after recognition of likely binding sites. A timestep of 1 fs is used in these simulations. Simulations were run for about 2 ns with different starting position of CO_2. All MD simulations are done using the LAMMPS code.[11] Corresponding analysis codes are self-written in FORTRAN 90.

The Grand Canonical Monte Carlo (GCMC) method is often adopted to understand and model gas adsorption in porous solids.[12] Here, we try to model CO_2 uptake in

SIFSIX-3-Cu using this technique. GCMC simulations reported here have been carried out using a code developed in-house.[13] In these simulations, the volume of the simulation cell and temperature were fixed and the chemical potential of the adsorbed phase was specified. The efficiency of the insertion move was particularly enhanced through the adoption of the cavity bias procedure.[14] Three-dimensional periodic boundary conditions were applied. To reduce computational costs, the GCMC simulations were carried out in a supercell of size 3 X 3 X 3 of the experimental SIFSIX-3-Cu unit cell. Fugacity coefficients for each pressure were calculated using the Thermosolver software[15] at 298 K, the temperature at which experimental isotherms were obtained. Non-bonded interactions were considered within a spherical cut-off of 12.8 Å. The adsorption isotherm of CO_2 was calculated at 298 K. At each state point, $2.5x10^8$ production Monte Carlo cycles were performed, subsequent to $1x10^8$ cycles devoted to equilibration. As in the case of classical MD simulations, UFF[6] parameters are used for MOF atoms and TraPPE parameters are considered for CO_2.[5] Cross terms are calculated using Lorentz-Berthelot combination rules. The atoms of the MOF are assumed to be neutral in charge. Nonetheless, good agreement with experiment is obtained.

To find the optimal locations of CO_2 molecules inside each of the respective frameworks, periodic density functional theory (DFT) calculations were carried out using the QUICKSTEP module in the CP2K software.[16] Valence electrons were treated in a mixed basis set with a plane wave energy cut-off of 280 Ry. The short-range version of the double- single polarization basis set was used. The effect of core electrons and nuclei was considered by using the norm-conserving pseudo-potentials of Goedecker-Teter-Hutter (GTH).[17] The exchange and correlation interactions between electrons were treated with the Perdew-Burke-Ernzerhof (PBE) functional.[18] van der Waals interactions between the gas and the framework are very important and, therefore, their effects were accounted for by employing empirical corrections prescribed by

Grimme.[19] We used the DFT-D3 scheme to calculate the cell volume in each of the cases. The optimized cell parameters are shown in the subsequent section. Calculations using the PBE functional along with D3 van der Waals corrections reproduced the experimental cell parameters within acceptable error limits. Geometry optimization was carried out with an appropriate number of CO_2 molecules introduced into the formula unit of the MOF. The binding energy between gas molecules and linkers of the MOF was calculated in the following manner:

$$\Delta E = E_{mof+gas} \text{ - } E_{mof} \text{ - } E_{gas}$$

where $E_{mof+gas}$ is the energy of the MOF with one molecule of CO_2, E_{mof} is the energy of the MOF and E_{gas} is the energy of the isolated gas molecule calculated in the same simulation cell as the MOF. During geometry optimization, component of forces on every atom was less than 10^{-4} a.u. Basis superposition errors (BSSE) in the energy are corrected using the counterpoise method.[20]

Born-Oppenheimer molecular dynamics calculations are also carried out using QUICKSTEP module[16] which uses a mixed basis set in which Kohn-Sham orbitals[21,22] are expanded in a Gaussian type atom-centered basis set while the electron density is represented using auxiliary plane wave basis set. All other details being the same as above, these simulations are run at 273 K in a few selected cases to better understand the architecture around possible binding sites. Nosé-Hoover thermostat[8] is used to control the temperature of the system. In all ab initio calculations, a super cell of size 2 X 2 X 2 of the experimental unit cell in used in the case of SIFSIX-3-Cu. In all other cases, a super cell of 1 X 1 X 2 of the experimental unit cell is used.

All structure visualisation was carried out using VMD,[23] Gaussview[24] and Mercury.[25]

3.3 Results and Discussions

3.3.1 Cell parameter optimization

All four MOFs have similar crystal structures and the corresponding units cells are primitive orthorhombic. The experimentally obtained desolvated structures of the four MOFs in consideration are used as a starting point for optimization of cell parameters. Symmetry present in the experimental unit cell parameters of each MOF is maintained in the supercell used for cell parameter optimization in each case. We relax the cell parameters through DFT-based geometry optimizations and we find reasonable agreement between the experimental and optimized cell parameters. We attribute deviations in cell volume to distortions in the heterocyclic rings of the linkers particularly in the first three cases. However, distortions are not very significant and, therefore, we have continued with the experimentally obtained cell parameters in simulations. The difference between the volumes obtained experimentally and theoretically are within an error limit of 5 % in each case and are indicated below in Tables 3.2-3.5.

Table 3.2: Optimization of cell parameters in SIFSIX-1-Cu

Method	a (Å)	b (Å)	c (Å)	α°	β°	γ°	V (Å)^3)
Experiment	11.045	11.045	16.326	90.00	90.00	90.00	1991.642
DFT	11.145	11.145	16.276	90.00	90.00	90.00	2021.659

Table 3.3: Optimization of cell parameters in SIFSIX-1'-Cu

Method	a (Å)	b (Å)	c (Å)	α°	β°	γ°	V (Å)^3)
Experiment	18.847	18.847	15.995	90.00	90.00	90.00	5681.635
DFT	18.957	18.957	16.375	90.00	90.00	90.00	5884.711

Table 3.4: Optimization of cell parameters in SIFSIX-2-Cu

Method	a (Å)	b (Å)	c (Å)	α°	β°	γ°	V $(Å)^3$)
Experiment	13.632	13.632	15.936	90.00	90.00	90.00	2961.236
DFT	13.742	13.742	16.326	90.00	90.00	90.00	3082.864

Table 3.5: Optimization of cell parameters in SIFSIX-3-Cu

Method	a (Å)	b (Å)	c (Å)	α°	β°	γ°	V $(Å)^3$)
Experiment	13.837	13.837	15.812	90.00	90.00	90.00	3027.532
DFT	13.747	13.747	15.572	90.00	90.00	90.00	2942.920

3.3.2 Binding sites

Adsorption sites in each of the MOFs considered here can easily be determined by inspection of the respective pore surfaces. All the MOFs considered here are square shaped grids and in the absence of open metal sites, primary interactions are between CO_2 and the SIFSIX pillars. Additionally, there may exist π-π interactions between the heterocyclic rings and CO_2. Adsorption sites, pore environment and binding energies are very similar in SIFSIX-1-Cu, SIFSIX-1'-Cu and SIFSIX-2-Cu. For the sake of completeness, we locate binding sites and calculate corresponding binding energies in each of the MOFs. The square shaped pores are lined by F functionalities in all three cases as shown in Figure 3.2.

Adsorption sites in SIFSIX-3-Cu were identified using both classical molecular dynamics simulations and DFT-based geometry optimizations. Calculations based on DFT were used to obtain an insight into the interaction between the gas molecule and the organic linkers present in the MOF. To identify adsorption sites in the other three MOFs, geometry optimizations have been sufficient to yield reasonably good agreement with experimental results. Dominant interactions between the adsorbed CO_2 and linkers of the MOF are almost identical in SIFSIX-1-Cu, SIFSIX-1'-Cu and SIFSIX-2-Cu owing to the structural similarity although the trends observed experimentally are captured in the calculations presented. Lewis acid-base interactions between CO_2 and SIFSIX groups seem to the most important interactions in these

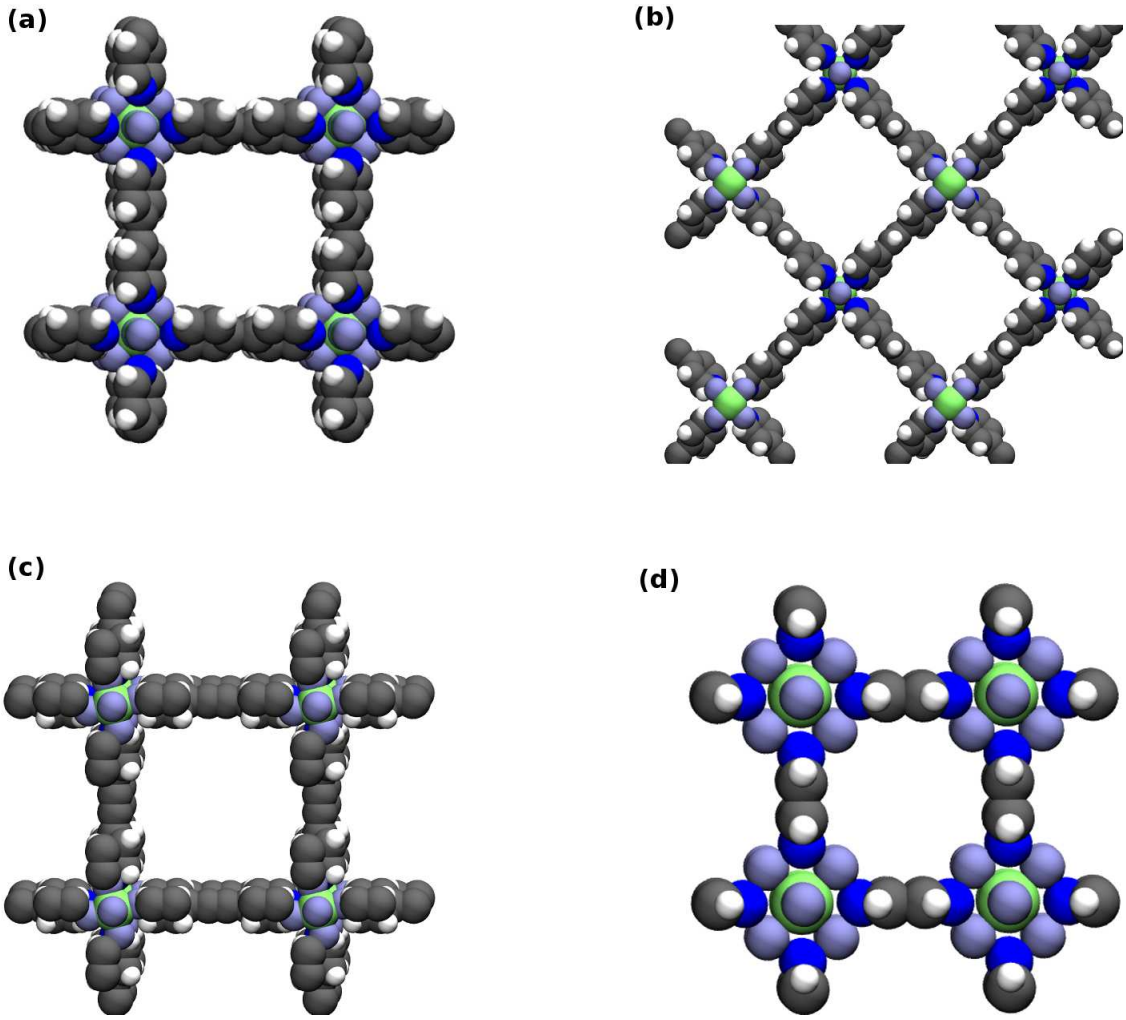

Figure 3.2: Pore architecture and chemical environments viewed along the c axis in (a) SIFSIX-1-Cu, (b) SIFSIX-1'-Cu, (c) SIFSIX-2-Cu and (d) SIFSIX-3-Cu. Color codes for MOF atoms: grey - C, blue - N, white - H, Green - Cu, ice blue - F, lime - Si.

MOFs. In SIFSIX-3-Cu, there are many more interactions and these are detailed below. Most likely binding sites for CO_2 are shown following which binding energies are discussed.

The specific nature of the interaction between the adsorbed CO_2 and the linkers of the framework can be best understood by looking at electron density differences within the region of interest. In general, two types of interactions have been identified between CO_2 and ligands of the SIFSIX-Cu MOFs: (i) π-π interactions between the aromatic rings and electron cloud of CO_2 and (ii) Lewis acid-base interactions

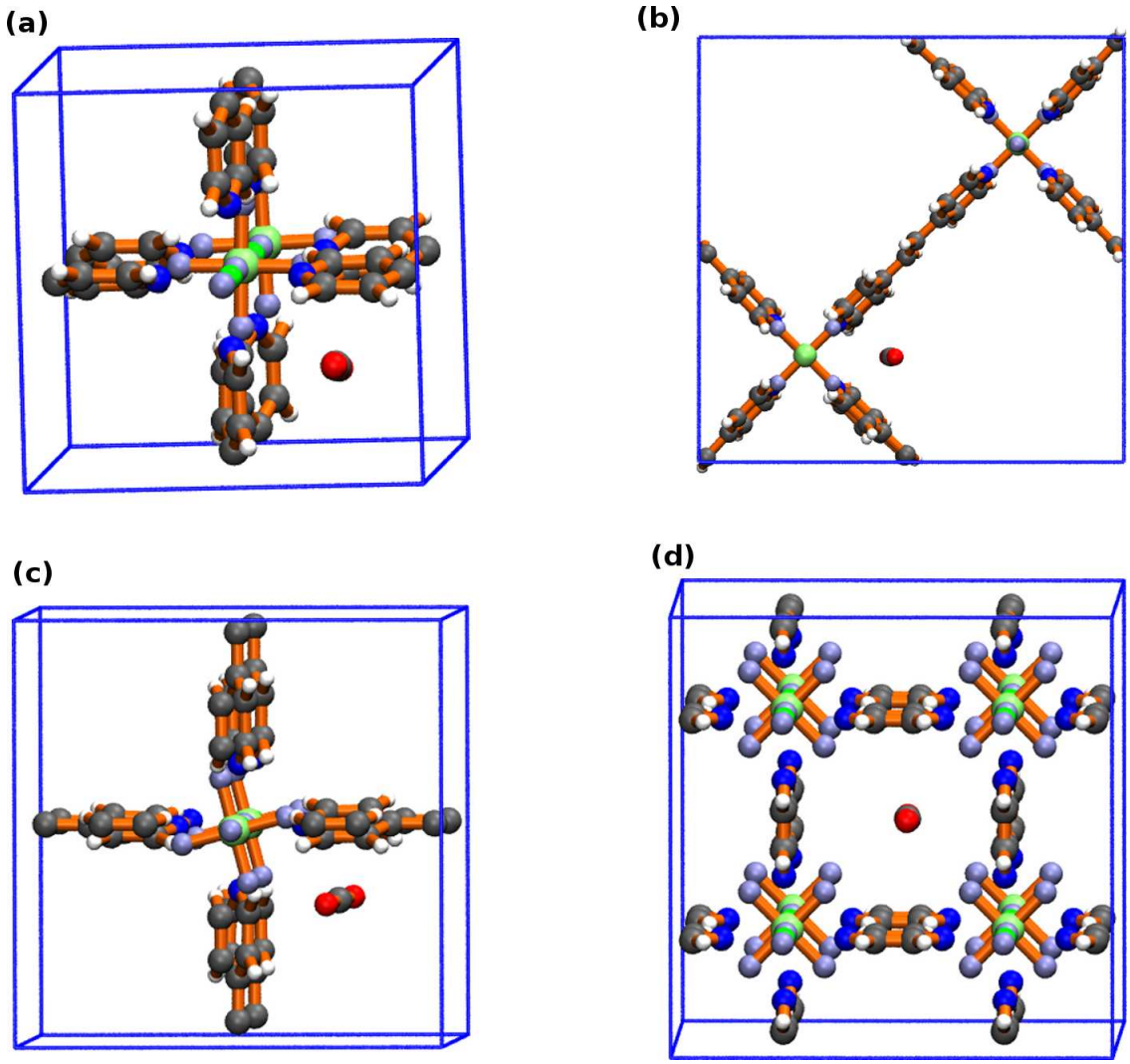

Figure 3.3: Binding sites for CO_2 in (a) SIFSIX-1-Cu, (b) SIFSIX-1'-Cu, (c) SIFSIX-2-Cu and (d) SIFSIX-3-Cu. Color codes for MOF atoms: grey - C, blue - N, white - H, Green - Cu, ice blue - F, lime - Si while carbon and oxygen in CO_2 are shown in grey and red respectively.

between the electron deficient carbon and fluorine in the SIFSIX units. In principle, there are several equivalent binding sites possible in SIFSIX-1-Cu, SIFSIX-1'-Cu and SIFSIX-2-Cu. Preliminary identification of binding sites in SIFSIX-3-Cu is obtained through MD simulations at sufficiently low temperatures to allow the inserted molecules to sample the complete pore environment within the MOF. The resulting configurations are then optimized using DFT-based methods and ab initio MD simulations were carried out to explore the region of interest. In the supercell we

have used, there is only one binding site possible per unit cell according to our calculations. Favourable binding sites for CO_2 adsorption are shown in all four MOFs considered here in Figure 3.3. SIFSIX-3-Cu shows the best promise for CO_2 capture both in terms of uptake and energetics and, therefore, particular attention is given to SIFSIX-3-Cu to understand CO_2 binding. The various binding energies obtained within the PBE/D3 level of theory and comparison with experiment are shown in Table 3.6. All experimental isosteric heats are determined at 273 and 298 K.

Table 3.6: Binding energies in the SIFSIX-Cu-MOFs

MOF	DFT (kJ/mol)	Experiment (kJ/mol)
SIFSIX-1-Cu	-30.99	-27
SIFSIX-1'-Cu	-29.66	-21
SIFSIX-2-Cu	-27.16	-22
SIFSIX-3-Cu	-60.56	-54

The binding site for CO_2 shown in SIFSIX-3-Cu is obtained easily through classical MD simulations. The most favourable adsorption site is at the centre of the tetragonal unit cell and there is a sharp minimum in potential energy obtained in this region. Binding energy for CO_2 adsorption in SIFSIX-3-Cu is overestimated with the DDEC method as seen earlier. However, trends are consistent and it allows for easy identification and verification of likely sites of adsorption. Better comparison with experimental results is obtained with DFT calculations as shown in Table 3.6.

Table 3.7: Binding energies calculated in SIFSIX-3-CU

Classical MD (kJ/mol)	DFT (kJ/mol)	Experiment (kJ/mol)
-71.9218	-60.56	-54

From electron density differences, various interactions possible between CO_2 and the linkers of the SIFSIX-Cu MOFs are elucidated for the adsorption sites discussed. As mentioned earlier, Lewis acid-base interactions between C of CO_2 and F present in the linkers of the MOFs are the dominant interactions in SIFSIX-1-Cu, SIFSIX-1'-Cu and SIFSIX-2-Cu as shown in Figure 3.4. The interactions observed are very

similar as shown and, therefore, binding energies are largely comparable with minor variations because of the topology of the MOFs. It is, therefore, understandable that uptake in these MOFs is also comparable with differences attributed to variations in pore dimensions.

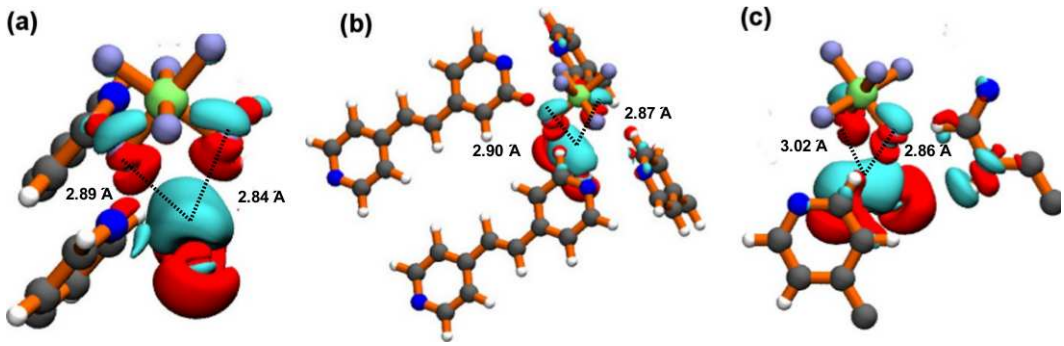

Figure 3.4: CO_2 interacting with linkers of (a) SIFSIX-1-Cu, (b) SIFSIX-1'-Cu and (c) SIFSIX-2-Cu. Cyan and red regions indicate decreased and increased electron densities, respectively, with respect to the isolated MOF and the isolated gas molecule. Isosurface value is 4 X 10^{-4} a.u. Color codes for MOF atoms: grey - C, blue - N, white - H, Green - Cu, ice blue - F, lime - Si while carbon and oxygen in CO_2 are shown in grey and red respectively.

In SIFSIX-3-Cu, the pore architecture affords many interactions between the adsorbed CO_2 molecule and the pyrazine rings as well as F atoms pointing into the pore. Lewis acid-base interactions are present between CO_2 and 4 F atoms from various SIFSIX units as well as π-π interactions owing to presence of the pyrazine rings present symmetrically. This is depicted in Figure 3.5. The interactions are very similar to those observed in SIFSIX-3-Zn expect that the pore size has been tuned leading to smaller distances between CO_2 and the various linkers present and, therefore, interactions are stronger leading to a higher binding energy.

3.3.3 Ab initio molecular dynamics simulations

As discussed previously, ab initio MD simulations are performed around the binding sites in two of the MOFs at 273 K keeping the framework fixed to explore regions around CO_2 binding sites. Given that the topology and adsorption sites for CO_2 are

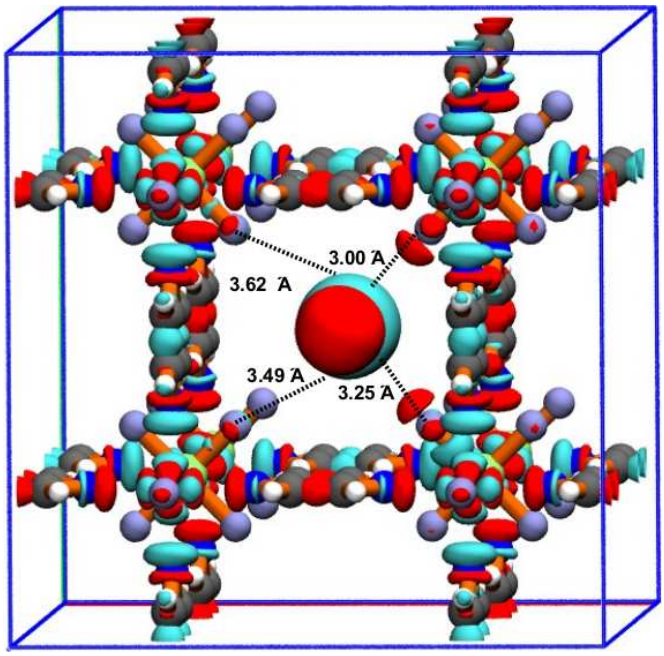

Figure 3.5: CO_2 interacting with linkers of SIFSIX-3-Cu. Cyan and red regions indicate decreased and increased electron densities, respectively, with respect to the isolated MOF and the isolated gas molecule. Isosurface value is 4 X 10^{-4} a.u. Color codes for MOF atoms: grey - C, blue - N, white - H, Green - Cu, ice blue - F, lime - Si while carbon and oxygen in CO_2 are shown in grey and red respectively.

Table 3.8: Structural differences in various SIFSIX-Cu-MOFs.

MOF	CO_2-aromatic ring (centroid) distances (Å)	CO_2-F distances (Å)	Δ H: DFT (kJ/mol)
SIFSIX-1-Cu	4.03, 4.37	2.84, 2.89	-30.99
SIFSIX-1'-Cu	4.14, 5.21	2.90, 2.87	-29.66
SIFSIX-2-Cu	3.55, 3.91	3.22, 2.76	-27.16
SIFSIX-3-Cu	4.27, 4.36, 4.55, 4.59	3.00, 3.25, 3.49, 3.62	-60.56
SIFSIX-3-Zn[26]	4.53, 4.53, 4.53, 4.53	3.39, 3.39, 3.39, 3.39	-48.03

similar in the bipyridine based SIFSIX-Cu MOFs, simulations are carried out only for SIFSIX-2-Cu to illustrate that the most favourable binding site involves Lewis acid-base interactions between CO_2 and 2 F atoms of the linkers as shown. It should

be noted that there is significant distortion in the framework with temperature owing to the long bipyridyl linkers. However, results consistent with experimental heats of adsorption are obtained in each case and, therefore, we proceed with fixed MOF simulations. The trajectory of only the centre of mass of the CO_2 molecule is shown for clarity in Figure 3.6a. Figure 3.6b confirms that adsorption site arrived at through geometry optimizations is indeed the energy minimum in that region. The binding energy corresponding to the minimum in Figure 3.6b is about 40 kJ/mol. This is higher than the value obtained earlier. This is probably because the MOF is held fixed in these simulations and we notice significant distortions in the heterocyclic linkers of the MOF upon introduction of CO_2 into framework while optimizing the respective geometries.

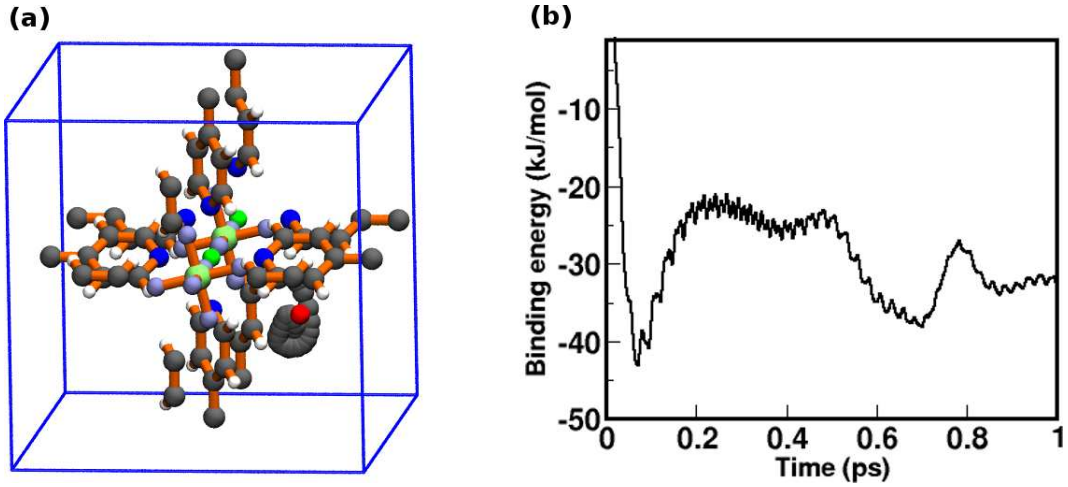

Figure 3.6: (a) Trajectory of CO_2 in SIFSIX-2-Cu around the adsorption site at 273 K with the MOF held fixed. (b) Binding energy of CO_2 adsorption in SIFSIX-2-Cu calculated along the trajectory near the F atoms of the SIFSIX pillars. Color codes for MOF atoms: grey - C, blue - N, white - H, Green - Cu, ice blue - F, lime - Si while carbon and oxygen in CO_2 are shown in grey and red respectively.

Ab initio MD simulations are also carried out for CO_2 adsorption in SIFSIX-3-Cu with the MOF held fixed. The simulation is carried out at 273 K around the indicated binding site determined through geometry optimization. The trajectory of the centre of mass of the CO_2 molecule shown in Figure 3.7a indicates that the

adsorbed CO_2 oscillates about the indicated binding site. The structure of SIFSIX-3-Cu is almost cubic with one side slightly larger than the others as in the case of the earlier reported SIFSIX-3-Zn. Indeed, the binding site for CO_2 in SIFSIX-3-Cu is found to be the same as in SIFSIX-3-Zn with greater interactions and binding energies. Binding energy is calculated along the trajectory and despite significant distortions of the pyrazine ring when the MOF is relaxed, we get a reasonable agreement with experimental binding energies as shown in Figure 3.7b. The binding energy calculated along the trajectory also confirms that the binding site predicted corresponds to an energy minimum in the region with the binding energy increasing as the CO_2 molecules moves on either side. This suggests that CO_2 binds at the centre of the simulation cell shown in Figure 3.7a to facilitate maximum interactions with linkers of SIFSIX-3-Cu and the dimensions of the cell are such that only one CO_2 molecule binds per unit cell. This is also verified through GCMC simulations.

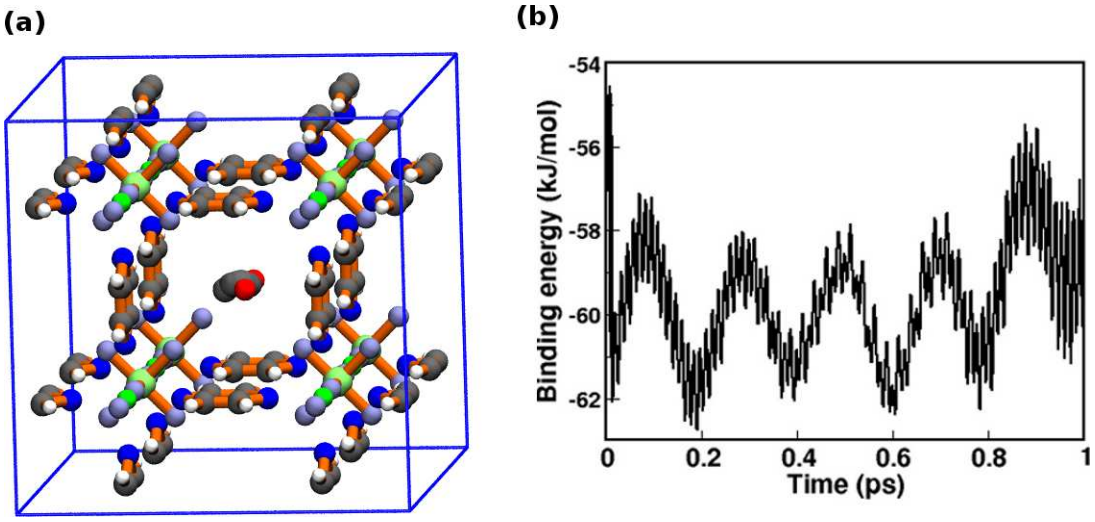

Figure 3.7: (a) Trajectory of CO_2 in SIFSIX-3-Cu around the adsorption site at 273 K with the MOF held fixed. (b) Binding energy of CO_2 adsorption in SIFSIX-3-Cu calculated along the trajectory indicated. Color codes for MOF atoms: grey - C, blue - N, white - H, Green - Cu, ice blue - F, lime - Si while carbon and oxygen in CO_2 are shown in grey and red respectively.

3.4 GCMC simulations

CO_2 uptake in SIFSIX-3-Cu is modelled using a GCMC code developed in-house as described earlier. A supercell of size 3 X 3 X 3 of the experimental unit cell is used and simulations are performed at 298 K for a range of pressure values for comparison with the experimentally obtained isotherms. Initially, only insertion of CO_2 molecules is carried out till a number, appropriate to the pressure at which the simulation is carried out, is reached. The simulation is run long enough to ensure equilibration and the mean values of uptake are considered and shown in Table 3.9.

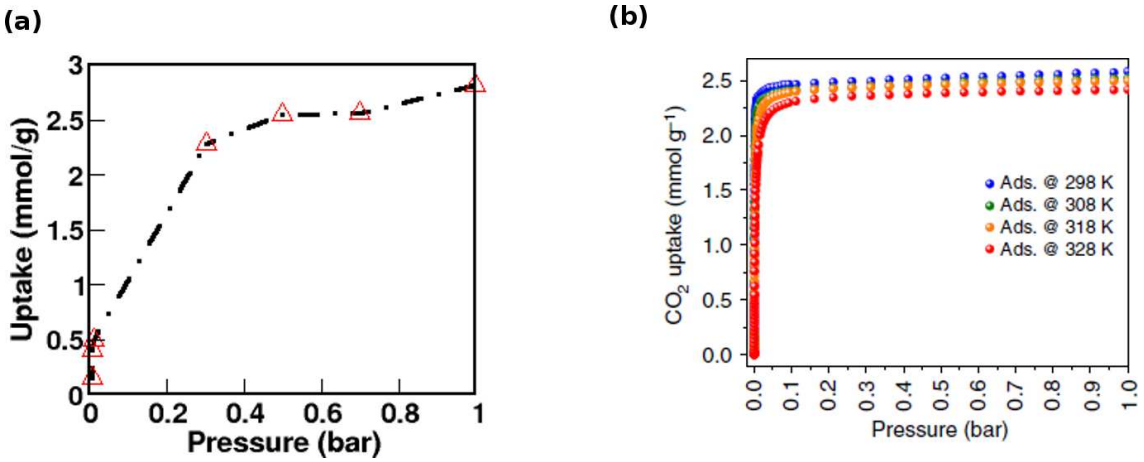

Figure 3.8: (a) Simulated uptake of CO_2 at 298 K in SIFSIX-3-Cu with data points marked. (b) Experimental isotherm of CO_2 for a range of temperatures in SIFSIX-3-Cu.[4]

Table 3.9: GCMC simulation of CO_2 adsorption in SIFSIX-3-CU

Pressure (bar)	Simulated uptake (mmol/g)	Number of CO_2 molecules
0.005	0.15144	3
0.008	0.410507	4
0.01	0.495621	5
0.3	2.28368	23
0.5	2.551	25
0.7	2.5538	25
1	2.81094	27

The isotherm obtained through GCMC simulations is in reasonable agreement with the experimental isotherm as shown in Figure 3.8a. The uptake calculated at 1 bar

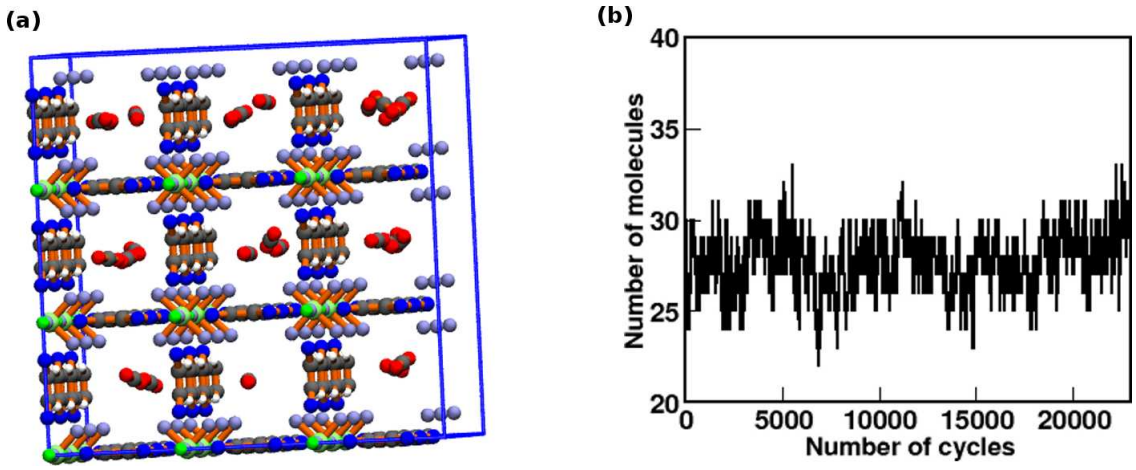

Figure 3.9: (a) CO_2 in a 3 X 3 X 3 unit cell of SIFSIX-3-Cu showing a maximum uptake of 27 molecules at 1 bar and 298 K. (b) Fluctuations in the number of CO_2 molecules in the GCMC simulation at 1 bar and 298 K.

corresponds to 27 molecules of CO_2 which suggests that indeed one CO_2 molecule is adsorbed per unit cell for maximum possible uptake since we have considered 27 unit cells in total here. In summary, adsorption in SIFSIX-3-Cu is reasonably well modelled. The sharp increase in uptake with pressure is well brought out explaining the high isosteric heat. Figure 3.9 shows CO_2 adsorption in the simulation cell taken compared with experimental results. Maximum possible uptake is 27 molecules for this supercell. This explains why the uptake saturates beyond this pressure.

3.5 Conclusions

We have attempted to model CO_2 adsorption in a class of SIFSIX-Cu MOFs showing promising CO_2 uptake and explain it in terms of pore architecture and functionalities. Given that predicting trends in gas adsorption with the functionalization of linkers is not trivial, these calculations help in understanding important consequences pore surface fluorination.

The current study also highlights the importance of engineering pore dimensions. An effort has also been made to theoretically explain the enhanced carbon capture in

SIFSIX-3-Cu. The binding site and energies predicted are in reasonable agreement with experimental data and, therefore, we believe these calculations indeed explain phenomena inherent in the topology of these porous solids.

Classical MD simulations carried out with charges derived from DFT-based methods predict trends in binding energies correctly even though the values are a little higher than experimental values. Trajectories predicted are in good agreement with intuition and experimental observations.

Ab initio calculations carried out helped in the determination of binding sites and trends in isosteric heat that are not obvious. It is extremely interesting that minute changes in the linkers of the framework can lead to 'made to order' frameworks with desirable carbon capture properties.

GCMC simulations have modelled CO_2 uptake in SIFSIX-3-Cu in decent agreement with experimental data thus confirming the CO_2 binding behaviour hypothesized during ab initio calculations. As seen from Table 3.8, CO_2-F distances tuned to about 3 to 3.5 $\mathring{A}$ with aromatic pyrazine rings surrounding the adsorbed molecule at a diatance of about 4.2 to 4.5 $\mathring{A}$ lead to enhanced adsorption and energetics in SIFSIX-3-Cu.

It is our belief and hope that these studies will lead to better efforts in developing porous frameworks drawing inspiration from theoretical results on existing porous solids.

Bibliography

[1] Burd, S. D.; Ma, S.; Perman, J. A.; Sikora, B. J.; Snurr, R. Q.; Thallapally, P. K.; Tian, J.; Wojtas, L.; Zaworotko, M. J. *Journal of the American Chemical Society* **2012**, *134*, 3663–3666.

[2] Nugent, P.; Belmabkhout, Y.; Burd, S. D.; Cairns, A. J.; Luebke, R.; Forrest, K.; Pham, T.; Ma, S.; Space, B.; Wojtas, L. et al.Nugent, Patrick and Belmabkhout, Youssef and Burd, Stephen D and Cairns, Amy J and Luebke, Ryan and Forrest, Katherine and Pham, Tony and Ma, Shengqian and Space, Brian and Wojtas, Lukasz and others *Nature* **2013**, *495*, 80–84.

[3] Uemura, K.; Maeda, A.; Maji, T. K.; Kanoo, P.; Kita, H. *European Journal of Inorganic Chemistry* **2009**, *2009*, 2329–2337.

[4] Shekhah, O.; Belmabkhout, Y.; Chen, Z.; Guillerm, V.; Cairns, A.; Adil, K.; Eddaoudi, M. *Nature communications* **2014**, *5*, 1–7.

[5] Potoff, J. J.; Siepmann, J. I. *AIChE Journal* **2001**, *47*, 1676–1682.

[6] Rappe, A. K.; Casewit, C. J.; Colwell, K. S.; Goddard, W. A.; Skiff, W. M. *Journal of the American Chemical Society* **1992**, *114*, 10024–10035.

[7] Manz, T. A.; Sholl, D. S. *Journal of Chemical Theory and Computation* **2012**, *8*, 2844–2867.

[8] Hoover, W. G. *Phys. Rev. A* **1985**, *31*, 1695–1697.

[9] Jones, J. E. *Proceedings of the Royal Society of London. Series A* **1924**, *106*, 463–477.

[10] Hockney,; Eastwood, *Computer Simulation Using Particles*; Taylor and Francis, 1988.

[11] Plimpton, S. *Journal of Computational Physics* **1995**, *117*, 1 – 19.

[12] Snurr, R. Q.; Bell, A. T.; Theodorou, D. N. *The Journal of Physical Chemistry* **1993**, *97*, 13742–13752.

[13] Bonakala, S.; Balasubramanian, S. *Submitted* **2015**.

[14] Kim, J.; Smit, B. *Journal of Chemical Theory and Computation* **2012**, *8*, 2336–2343.

[15] Barnes, C. S. Ph.D. thesis, 2007.

[16] VandeVondele, J.; Krack, M.; Mohamed, F.; Parrinello, M.; Chassaing, T.; Hutter, J. *Computer Physics Communications* **2005**, *167*, 103 – 128.

[17] Goedecker, S.; Teter, M.; Hutter, J. *Phys. Rev. B* **1996**, *54*, 1703–1710.

[18] Perdew, J. P.; Burke, K.; Ernzerhof, M. *Physical review letters* **1996**, *77*, 3865.

[19] Grimme, S. *Journal of Computational Chemistry* **2006**, *27*, 1787–1799.

[20] Boys, S. F.; Bernardi, F. d. *Molecular Physics* **1970**, *19*, 553–566.

[21] Hohenberg, P.; Kohn, W. *Phys. Rev.* **1964**, *136*, B864–B871.

[22] Kohn, W.; Sham, L. J. *Phys. Rev.* **1965**, *140*, A1133–A1138.

[23] Humphrey, W.; Dalke, A.; Schulten, K. *Journal of Molecular Graphics* **1996**, *14*, 33–38.

[24] Dennington, R.; Keith, T.; Millam, J. *GaussView Version 5*, Semichem Inc. Shawnee Mission KS 2009.

[25] Bruno, I. J.; Cole, J. C.; Edgington, P. R.; Kessler, M.; Macrae, C. F.; McCabe, P.; Pearson, J.; Taylor, R. *Acta Crystallographica Section B: Structural Science* **2002**, *58*, 389–397.

[26] Kanoo, P.; Reddy, S. K.; Kumari, G.; Haldar, R.; Narayana, C.; Balasubramanian, S.; Maji, T. K. *Chem. Commun.* **2012**, *48*, 8487–8489.

Chapter 4

Modelling CO_2 adsorption in azine functionalized porous frameworks

4.1 Introduction

The previous chapters discussed the concept of rational design of tailoring porous frameworks for enhanced storage capacity and selectivity for CO_2. Here, we proceed in the same general direction to consider frameworks designed with azine functionalized pores. In general, tuning of functionalities of pores in MOFs can broadly be achieved through two means: (i) introduction of coordinatively unsaturated metal ions or (ii) introduction of Lewis basic groups. It has been reported that control over pore size of MOFs functionalized with azine groups enables enhanced interactions between CO_2 molecules and the framework. This chapter deals with understanding gas adsorption in two new three-dimensional (3D) azine functionalized Zn(II)-based MOFs isolated via mechanosynthesis.

The strategy adopted in the construction of these MOFs involves pillaring 2D layers comprising Zn(II) ions and the V-shaped 4,4-oxybisbenzoic acid (oba) ligand with linear pyridyl-based ligands.[1] The selected pillaring ligands used in the construction

of these MOFs are 1,4-bis(4-pyridyl)-2,3-diaza-1,3-butadiene (4-bpdb) and 2,5-bis(4-pyridyl)-3,4-diaza-2,4-hexadiene (4-bpdh) as shown in Figure 4.1 leading to TMU-4 and TMU-5 respectively. (TMU: Tarbiat Modares University)

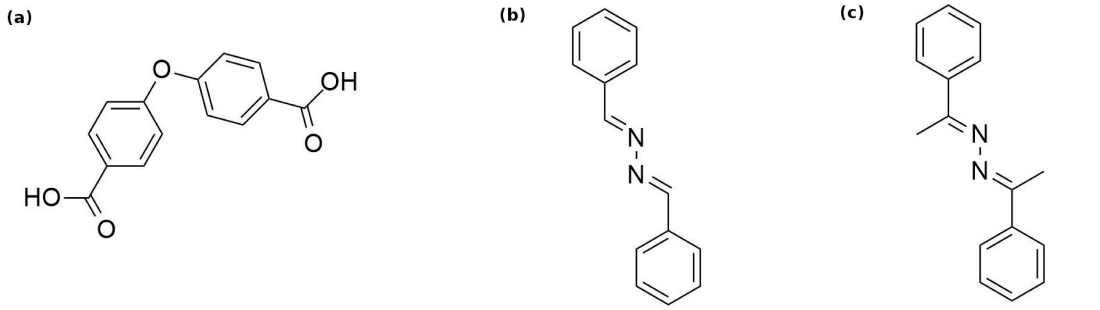

Figure 4.1: Chemical structure of (a) 4,4'-oxybisbenzoic acid, (b) 1,4-bis(4-pyridyl)-2,3-diaza-1,3-butadiene (4-bpdb) and (c) 2,5-bis(4-pyridyl)-3,4-diaza-2,4-hexadiene (4-bpdh)

Pores of MOFs constructed from layers pillared by linear ligands are usually delimited by these ligands. The ligands used contain a bridging azine group in the middle. Therefore, it was expected and confirmed that the pores of the MOFs should contain two internal Lewis basic sites per ligand. TMU-4 shows relatively larger 1D pores (size: 6.8 X 7.8 Å, including van der Waals radii), whereas TMU-5 shows interconnected, narrow 3D pores (size: 5.6 X 3.8 Å, including van der Waals radii). It is observed that the combination of pore size and pore functionalization with azine groups favour the host-CO_2 interactions. We try to understand from a theoretical perspective how use of marginally different N-donor ligands leads to frameworks with different topologies, pore sizes and accessible volumes.

TMU-4 is based on a binuclear Zn_2 unit in which both tetrahedral Zn(II) centers are coordinated to three O atoms from carboxylate groups of deprotonated oba ligands and one N atom. Each oba ligand binds three consecutive Zn(II) centers from two different Zn_2 units thereby forming 2D sheets. The linear 4-bpdb connects the 2D sheets extending the structure in three dimensions. TMU-4 is doubly interpenetrated, but it still contains 1D pore channels with the internal surface functionalized

with azine groups. TMU-5 is very similar in construction except that the pyridyl-based linker used is 4-bpdh. The introduction of two methyl groups in the N-donor pillar ligand produces a different structure based on a binuclear paddlewheel Zn(II) unit in which four O atoms from carboxylate groups of oba form an approximate equatorial square plane. Each Zn(II) center is coordinated to one N atom from 4-bdph. The oba ligands orient themselves around the paddlewheel unit forming 2D layers wich are pillared by 4-bpdh to yield a 3D framework. TMU-5 contains narrower channels than TMU-4 and these channels are also functionalized with azine groups. Even though TMU-5 has smaller pores than TMU-4, it is porous to CO_2 at 1 bar and 195 K. CO_2 isotherms at 195 K collected at 1 bar and 195 K indicate a marginally higher uptake in the case of TMU-4.[1] However, isotherms at 273 K and low pressures indicate higher uptake in TMU-5 indicating enhanced interactions in TMU-5. Isosteric heat for CO_2 adsorption calculated at 273 K and 298 K is higher in the case of TMU-5.

In the following, likely binding sites are easily identified on the basis of functionalities present. We then proceed to use ab initio methods to explore regions near functional groups and calculate corresponding binding energies. The dominant interaction present here is Lewis acid-base interactions between the linkers of the TMU MOFs and C of CO_2. Apart from this, an attempt is made to model uptake in the TMU MOFs using GCMC simulations. We try to understand through classical and ab initio methods how pore architecture can be designed for effective CO_2 capture.

The experimentally obtained desolvated structures are used as a starting point in these calculations. The central focus of this work is understanding CO_2 uptake in the TMU MOFs and, therefore, we place emphasis on GCMC modelling of CO_2 adsorption and achieving reasonable agreement with experimental isotherms. The systems and methods used are described further in the subsequent sections.

4.2 Computational Details

Calculations reported here are carried out using both classical and ab initio methods. Binding sites are initially investigated using classical methods followed by ab initio calculation to determine binding energies and interactions. Finally, GCMC simulations are used to obtain theoretical isotherms for CO_2 adsorption for comparison with experimental data.

Classical molecular dynamics (MD) simulations are carried out in the canonical ensemble (constant NVT) to explore the pore surface and identify possible binding sites for CO_2 in the TMU MOFs. Partial charges and Lennard-Jones (LJ) parameters for CO_2 are taken from the TraPPE force field.[2] LJ parameters for the MOFs are taken from the Universal force field (UFF).[3] Partial charges are calculated using the 'Density derived electrostatic charges' (DDEC) method[4] from the valence electron densities and these are used to model electrostatic interaction between the linkers of the TMU MOFs and adsorbed CO_2 for evaluation of adsorption sites. Cross terms are calculated using the Lorentz-Berthelot mixing rules. Temperature of the system is maintained using Nosé-Hoover thermostat.[5] All classical simulations were performed with desolvated structures.

12-6 LJ functional[6] is used to calculate pairwise interactions in direct space within a cutoff distance of 12.8 Å. Above this distance, long-range electrostatic interactions are calculated in reciprocal space using particle-particle particle-mesh method with an accuracy of 1 part in 10^5.[7] The MOF is kept frozen in each of the simulations which obviates the need to develop intramolecular parameters for the MOF.

For preliminary identification of binding sites and calculation of heats of adsorption, the experimental unit cell is used in each case with charges derived from DFT- based methods. The simulation is performed at 20 K so that a randomly inserted CO_2 molecule can move slowly and sample the entire space within the MOF. Binding sites are identified by looking at the potential energy of the system with time. A

timestep of 1 fs is used in these simulations. Simulations were run for about 2 ns with different starting position of CO_2. All MD simulations are done using the LAMMPS code.[8] Once the most likely site corresponding to an energy minimum is determined, energy minimization is carried out starting from that location to estimate energies of adsorption. Corresponding analysis codes are self-written in FORTRAN 90.

As described in the previous chapter, GCMC modelling is a useful tool to understand gas adsorption in porous solids. GCMC simulations here have been carried out using a code developed in-house.[9] In these simulations, the volume of the supercell and temperature were fixed and the chemical potential of the adsorbed phase was specified. Three-dimensional periodic boundary conditions were applied. To reduce computational costs, the GCMC simulations were carried out in a supercell of size 2 X 1 X 2 of the experimental unit cell for TMU-4 and that of size 1 X 2 X 2 of the experimental unit cell cell for TMU-5. Fugacity coefficients for each pressure were calculated using the Thermosolver software[10] at 195 K, the temperature at which experimental isotherms were obtained. Non-bonded interactions were considered within a spherical cut-off of 12.8 Å. The adsorption isotherm of CO2 was calculated at 195 K. At each state point, $2.5x10^8$ production Monte Carlo cycles were performed, subsequent to $1x10^8$ cycles devoted to equilibration.

As in earlier cases, UFF[3] parameters are used for MOF atoms and TraPPE parameters are considered for CO_2.[2] Cross terms are calculated using Lorentz-Berthelot combination rules. Assuming atoms of the MOFs to be charge neutral leads to results reasonably comparable with experiment as illustrated earlier and, therefore, the same formalism is followed here.

For the determination of positions of CO_2 molecules inside each of the respective frameworks, periodic density functional theory (DFT) calculations were carried out using the QUICKSTEP module in the CP2K software.[11] Valence electrons were treated in a mixed basis set with a plane wave energy cut-off equal to 280 Ry. The

short-range version of the double- single polarization basis set was used. The effect of core electrons and nuclei was considered by using the norm-conserving pseudopotentials of Goedecker-Teter-Hutter (GTH).[12] The exchange and correlation interactions between electrons were treated with the Perdew-Burke-Ernzerhof (PBE) functional.[13] van der Waals interactions between the gas and the framework are very important and, therefore, their effects were accounted for by employing empirical corrections prescribed by Grimme.[14] We used the DFT-D3 scheme to calculate the cell volume in each of the cases. The optimized cell parameters and volumes are shown in the subsequent section. Calculations using the PBE functional along with D3 van der Waals corrections reproduced the experimental cell parameters within resonable limits. Geometry optimization was carried out with an appropriate number of CO_2 molecules introduced into the formula unit of the MOF. The binding energy between gas molecules and linkers of the MOF was calculated in the following manner:

$$\Delta E = E_{mof+gas} \text{ - } \mathrm{E}_{mof} \text{ - } \mathrm{E}_{gas}$$

where $\mathrm{E}_{mof+gas}$ is the energy of the MOF with one molecule of CO_2, E_{mof} is the energy of the MOF and E_{gas} is the energy of the isolated gas molecule calculated in the same simulation cell as the MOF. During geometry optimization, component of forces on every atom was less than 10^{-4} a.u. Basis superposition errors (BSSE) in the energy are corrected using the counterpoise method.[15]

Born-Oppenheimer molecular dynamics calculations are also carried out using QUICKSTEP module[11] which uses a mixed basis set in which Kohn-Sham orbitals[16,17] are expanded in a Gaussian type atom-centered basis set while the electron density is represented using auxiliary plane wave basis set. All other details being the same as above, these simulations are run at 195 K in the case of TMU-5 to better understand the architecture around possible binding sites. Nosé-Hoover thermostat[5] is used to control the temperature of the system. For both MOFs considered here, the

experimental unit cell is used for ab initio calculations.

All structure visualisation was carried out using VMD,[18] Gaussview[19] and Mercury.[20]

4.3 Results and Discussions

4.3.1 Cell parameter optimization

Proceeding as in the previous chapters, the experimentally obtained desolvated structures of the two MOFs in consideration are used for optimization of cell parameters. Symmetry present in the experimental unit cell parameters of each MOF is maintained in each case. In the case of the TMU MOFs, this only involves constraining β to 90°. We relax the cell parameters through DFT-based geometry optimizations and we find reasonable agreement between the experimental and optimized cell parameters. Therefore, we have continued with the experimentally obtained cell parameters in simulations. The difference between the cell volumes obtained experimentally and theoretically are within acceptable error limits as indicated below in Tables 4.1-4.2.

Table 4.1: Optimization of cell parameters in TMU-4

Method	a (Å)	b (Å)	c (Å)	$\alpha°$	$\beta°$	$\gamma°$	V (Å)^3)
Experiment	12.546	26.633	15.734	90.00	97.87	90.00	5207.817
DFT	12.526	26.203	15.044	90.00	95.27	90.00	4916.859

Table 4.2: Optimization of cell parameters in TMU-5

Method	a (Å)	b (Å)	c (Å)	$\alpha°$	$\beta°$	$\gamma°$	V (Å)^3)
Experiment	26.808	8.192	23.302	90.00	98.96	90.00	5055.282
DFT	25.848	8.152	22.942	90.00	99.06	90.00	4774.197

4.3.2 Binding sites

An idea of adsorption sites in each of the MOFs considered here can be obtained by examining the respective pore surfaces. Both the TMU MOFs do not possess open metal sites and therefore, Lewis acid-base interactions are most likely between CO_2 and O atoms of the carboxylate groups or the bridging O atom present in the dicarboxylate ligand, oba. These interactions are also possible between CO_2 and N present in the azine linkers of the MOFs. Additionally, there may exist π-π interactions between CO_2 and various aromatic rings present in the ligands. Adsorption sites and pore environments are interestingly very different in the two MOFs. The addition of two methyl groups in the N-donor pillar ligand leads to significantly different pore architecture as shown in Figure 4.2. TMU-4 consists of larger one-dimensional (1D) pores while TMU-5 consists of smaller 3D pores.

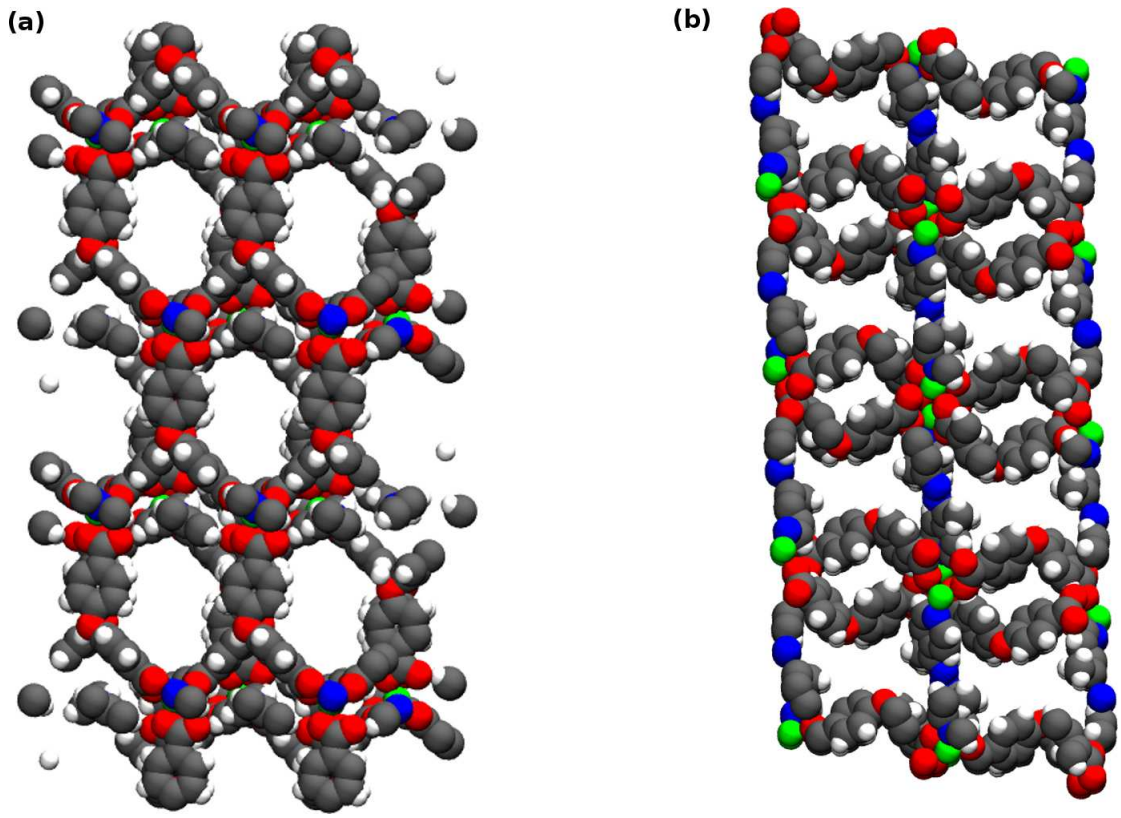

Figure 4.2: Pore architecture and chemical environments in (a) TMU-4 and (b) TMU-5. Color codes for MOF atoms: grey - C, blue - N, white - H, Green - Zn, Red -O.

Adsorption sites in both the TMU MOFs were identified using both classical molecular dynamics simulations and DFT-based geometry optimizations. Calculations based on DFT were used to obtain an insight into the interaction between the gas molecule and the organic linkers present in the MOF. To identify adsorption sites in TMU-4, geometry optimizations have been sufficient to yield reasonably good agreement with experimental results. However, experimentally obtained isosteric heats are not obtained for binding sites predicted in the case of TMU-5 and, therefore, ab initio molecular dynamics simulations are performed within the vicinity of probable adsorption sites in an attempt to understand these anomalies. Dominant interactions between the adsorbed CO_2 and linkers of the MOF are almost identical in TMU-4 and TMU-5 owing to the similarity of the linkers utilized in their construction as shown in Figure 4.3 although we find a slightly higher binding energy in TMU-5. Lewis acid-base interactions between CO_2 and O atoms present on the dicarboxylate ligands seem to the most important interactions in both these MOFs. There are multiple possible equivalent sites with these interactions and three of these are highlighted for TMU-4 in Figure 4.3a. The most likely binding site in TMU-5 is shown in Figure 4.3b.

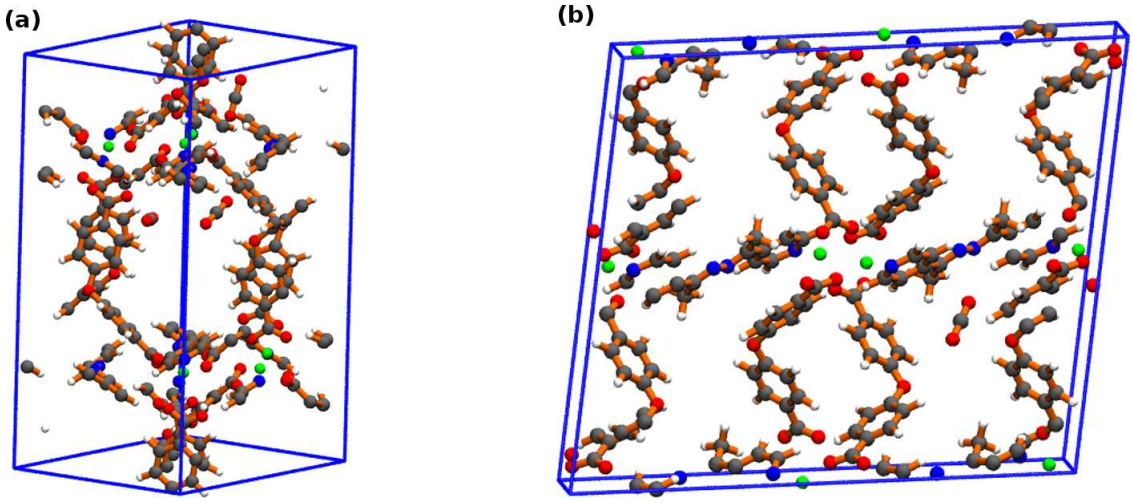

Figure 4.3: Binding sites for CO_2 in (a) TMU-4 and (b) TMU-5. Color codes for MOF atoms: grey - C, blue - N, white - H, Green - Zn, Red -O while carbon and oxygen in CO_2 are shown in grey and red respectively.

As illustrated earlier, the specific nature of the interaction between the adsorbed CO_2 and the linkers of the framework can be best understood by looking at electron density differences within the region of interest. In general, two types of interactions are broadly possible between CO_2 and the TMU MOFs: (i) π-π interactions between the various aromatic groups present in the linkers and electron cloud of CO_2 and (ii) Lewis acid-base interactions between the electron deficient carbon and electronegative atoms present in the ligands. In principle, there are several equivalent binding sites in both TMU MOFs. Preliminary identification of binding sites is obtained through MD simulations at sufficiently low temperatures to allow the inserted molecules to sample the complete pore environment within the MOF. The resulting configurations are then optimized using DFT-based methods. Very poor agreement with zero coverage isosteric heat obtained experimentally is observed in the case of TMU-5. It is worthwhile to note that the binding energy predicted theoretically matches well with heats of adsorption at slightly higher coverages. Ab initio MD simulations were carried out to explore the regions of interest to understand this deviation. It should be noted that the binding energy predicted for TMU-4 is in good agreement with experiment. TMU-4 shows the best promise for CO_2 capture in terms of uptake and energetics and, therefore, an effort is made to understand the reduced uptake in TMU-5. The various binding energies obtained within the PBE/D3 level of theory and comparison with experiment are shown in Table 4.3. All experimental isosteric heats are determined at 273 and 298 K.

Table 4.3: Binding energies for CO_2 in the TMU MOFs

MOF	DFT (kJ/mol)	Classical MD (kJ/mol)	Experiment (kJ/mol)
TMU-4	-28.33	-39.93	-25.6
TMU-5	-31.12	-40.48	-43.4

The binding sites shown in TMU-4 are obtained easily through classical MD simulations and are equivalent in terms of the chemical environments and energies. It is understandable that predicted binding sites are around O atoms instead of the

azine functionalities and there is a sharp minimum in potential energy obtained in this region. Binding energy for CO_2 adsorption in TMU-4 is overestimated with the DDEC method as seen in Table 4.3. However, the trend is consistent and it allows easy identification of both adsorption sites and energies. Better comparison with experimental results is obtained for TMU-4 through DFT calculations as shown in Table 4.3. TMU-5 possesses similar functionalities and, therefore, we expect binding sites with similar interactions. However, the binding energy predicted through DFT is slightly higher than that of TMU-4 probably because of smaller pores but much lower than those obtained experimentally, particularly at low coverages. It is not evident why this is observed.

From electron density differences, various interactions possible between CO_2 and the linkers of the TMU azine frameworks are elucidated for the adsorption sites discussed. As mentioned earlier, Lewis acid-base interactions between C of CO_2 and O present in the linkers of the MOFs are the dominant interactions in both cases. π-π interactions are also present as is evident from the electron density differences shown in Figure 4.4. Once again, we see that interactions observed in both MOFs are very similar in similar in nature. Minor differences arise simply because of the topology of the respective structures.

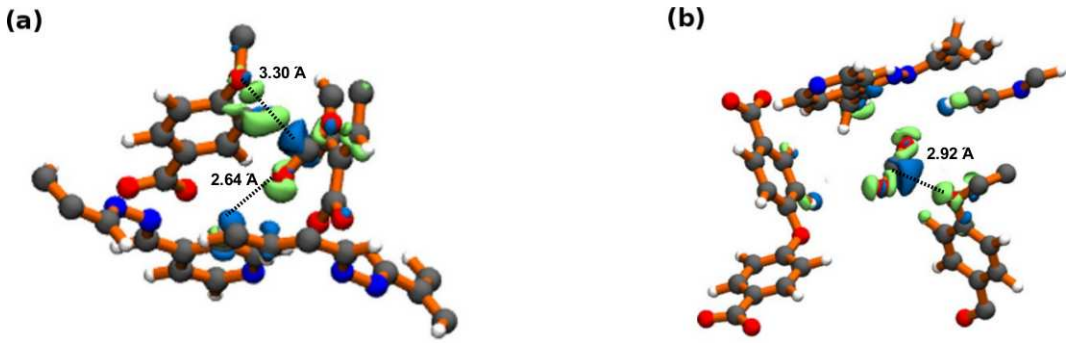

Figure 4.4: CO_2 interacting with linkers of (a) TMU-4 and (b) TMU-5. Cyan and lime regions indicate decreased and increased electron densities, respectively, with respect to the isolated MOF and the isolated gas molecule. Isosurface value is 4 X 10^{-4} a.u. Color codes for MOF atoms: grey - C, blue - N, white - H, Green - Zn, Red -O while carbon and oxygen in CO_2 are shown in grey and red respectively.

In TMU-5, the pore architecture is different with smaller dimensions and it is found from DFT calculations that there is a slightly higher binding energy for CO_2 adsorption than that predicted in TMU-4. However, it is interesting to note that very little direct interaction is observed between the adsorbed CO_2 molecules and the azine functionalities. Almost all MD simulations lead to energy minima with CO_2 bound near the carboxylate moiety.

4.3.3 Ab initio molecular dynamics simulations

As discussed previously, ab initio MD simulations are performed only in TMU-5 at 195 K keeping the framework fixed to explore regions around the CO_2 binding sites. Given that the adsorption sites for CO_2 in TMU-5 are similar in terms of chemical environment, simulations are carried out around the adsorption site indicated in Figure 4.3b to illustrate that the most favourable binding site involves Lewis acid-base interactions between CO_2 and the bridging O atom present in the dicarboxylate linker. We do not consider distortion of the framework with temperature and this may the key to understanding these discrepancies in binding energies. However, we obtain results consistent those obtained from geometry optimizations. The trajectory of only the centre of mass of the CO_2 molecule is shown for clarity in Figure 4.5a where the adsorbed molecule oscillates about the predicted binding site. Figure 4.5b confirms that adsorption site arrived at through geometry optimizations is indeed the energy minimum in that region. The binding energy corresponding to the minimum in Figure 4.5b is about 33 kJ/mol, a value slighter higher than that indicated in Table 4.3. This is probably because the MOF is held fixed in these simulations and we notice significant distortions in the heterocyclic linkers of the MOF upon introduction of CO_2 into framework while optimizing the respective geometries even at 0 K.

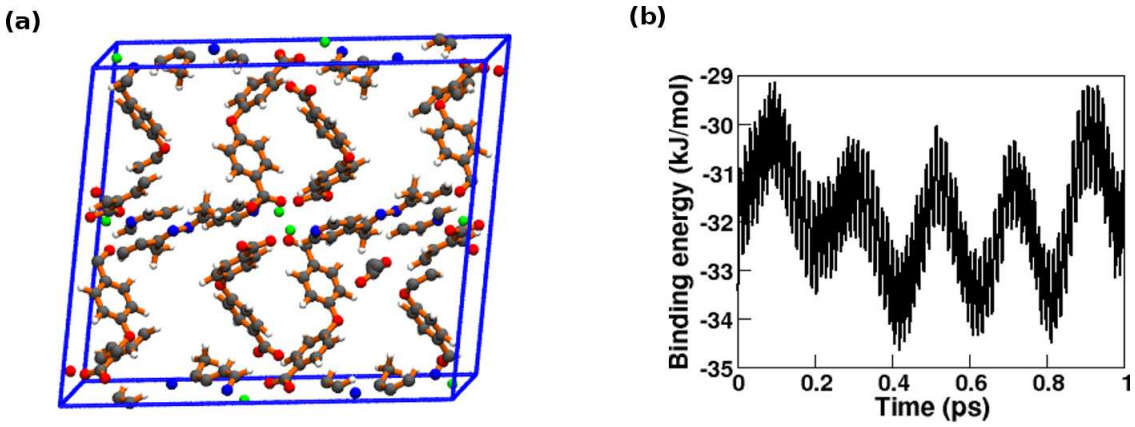

Figure 4.5: (a) Trajectory of CO_2 in TMU-5 around the adsorption site at 195 K with the MOF held fixed. (b) Binding energy of CO_2 adsorption in TMU-5 calculated along the trajectory near the O atoms of the carboxylate groups. Color codes for MOF atoms: grey - C, blue - N, white - H, Green - Zn, Red -O while carbon and oxygen in CO_2 are shown in grey and red respectively.

4.4 GCMC simulations

CO_2 uptake in the TMU MOFs is modelled using a GCMC code developed in-house as described earlier. In the case of TMU-4, a supercell of size 2 X 1 X 2 of the experimental unit cell is used and simulations are performed at 195 K for a range of pressure values for comparison with the experimentally obtained isotherms. In case of TMU-5, a supercell of size 1 X 2 X 2. Initially, only insertion of CO_2 molecules is carried out till a number appropriate to the pressure at which the simulation is carried out is reached. The simulation is run long enough to ensure equilibration and the mean values of uptake are considered and shown in Table 4.4. Figure 4.6 displays the isotherms obtained through GCMC and their comparison with experimental data.

The isotherm obtained through GCMC simulations are in reasonable agreement with the experimental isotherm as shown in Figure 4.6a. It is seen that TMU-4 shows a higher uptake than TMU-5 at most pressure values sampled owing to the larger pore dimensions. The uptake values are also in comparison with those obtained from the experimental isotherms. At very low pressures, it is experimentally observed that

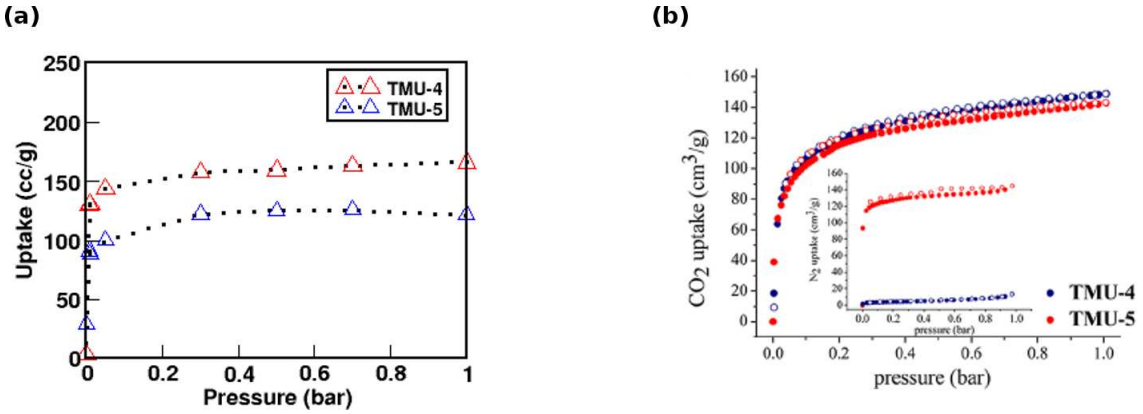

Figure 4.6: (a) Simulated uptake of CO_2 at 195 K in TMU MOFs with data points marked. (b) Experimental isotherm of CO_2 at 195 K in the TMU MOFs.[1]

Table 4.4: GCMC simulation of CO_2 adsorption in TMU MOFs

Pressure (bar)	Uptake: TMU-4 (cc/g)	Uptake: TMU-5 (cc/g)
0.0001	3.70	29.1087
0.008	129.72	90.75
0.01	130.52	88.41
0.05	143.52	99.95
0.3	157.44	122.15
0.5	159.36	125.09
0.7	162.76	125.72
1	165.78	121.44

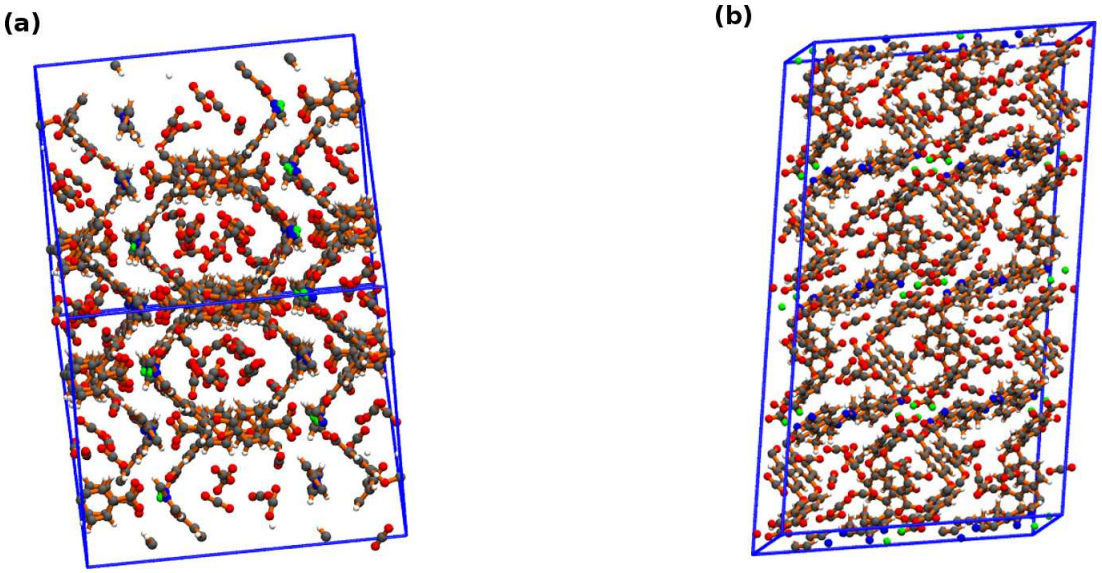

Figure 4.7: (a) CO_2 uptake in a 2 X 1 X 2 unit cell of TMU-4 at 1 bar and 298 K. (b) CO_2 uptake in a 1 X 2 X 2 unit cell of TMU-5 at 1 bar and 298 K.

TMU-5 shows a higher uptake. We observe this trend also which is explained by slightly enhanced interactions in TMU-5 owing to smaller pore dimensions. This fact is also supported by higher isosteric heats. Figure 4.7 shows the simulated adsorption of CO_2 molecules into the TMU MOFs. The snapshots are taken at 195 K and 1 bar. CO_2 adsorption is well modelled in the TMU MOFs.

4.5 Conclusion

We have tried to model CO_2 adsorption in a class of azine based MOFs showing promising CO_2 uptake and explain it in terms of pore architecture. It is interesting that minute functional variations lead to significantly different architectures and adsorption behaviour.

The current study also highlights the importance of engineering pore dimensions. An effort has also been made to theoretically explain the enhanced carbon capture in TMU-4. There exists a sensitive balance between isosteric heat of adsorption and uptake. We have verified here that higher isosteric heat does not necessarily correspond to a higher uptake at ambient conditions.

Classical MD simulations carried out with charges derived from DFT-based methods predict trends in binding energies correctly even though the values are a little higher than experimental values. Trajectories predicted are in good agreement with intuition and experimental observations.

Ab initio calculations carried out helped in the determination of binding sites and trends in isosteric heat that are not obvious. It is extremely interesting that minute changes in the linkers of the framework can lead to 'made to order' frameworks with desirable carbon capture properties. Differences in enthalpy are obtained from DFT calculations and experiment in the case of TMU-5 and, therefore, further studies are required.

GCMC simulations have modelled CO_2 uptake in the TMU MOFs in reasonable

agreement with experimental data thus confirming the CO_2 binding behaviour hypothesized during ab initio calculations.

In conclusion, we have tried to gain some understand into azine functionalization of pore surfaces and consequences on CO_2 adsorption properties.

Bibliography

[1] Masoomi, M. Y.; Stylianou, K. C.; Morsali, A.; Retailleau, P.; Maspoch, D. *Crystal Growth & Design* **2014**, *14*, 2092–2096.

[2] Potoff, J. J.; Siepmann, J. I. *AIChE Journal* **2001**, *47*, 1676–1682.

[3] Rappe, A. K.; Casewit, C. J.; Colwell, K. S.; Goddard, W. A.; Skiff, W. M. *Journal of the American Chemical Society* **1992**, *114*, 10024–10035.

[4] Manz, T. A.; Sholl, D. S. *Journal of Chemical Theory and Computation* **2012**, *8*, 2844–2867.

[5] Hoover, W. G. *Phys. Rev. A* **1985**, *31*, 1695–1697.

[6] Jones, J. E. *Proceedings of the Royal Society of London. Series A* **1924**, *106*, 463–477.

[7] Hockney,; Eastwood, *Computer Simulation Using Particles*; Taylor and Francis, 1988.

[8] Plimpton, S. *Journal of Computational Physics* **1995**, *117*, 1 – 19.

[9] Bonakala, S.; Balasubramanian, S. *Submitted* **2015**.

[10] Barnes, C. S. Ph.D. thesis, 2007.

[11] VandeVondele, J.; Krack, M.; Mohamed, F.; Parrinello, M.; Chassaing, T.; Hutter, J. *Computer Physics Communications* **2005**, *167*, 103 – 128.

[12] Goedecker, S.; Teter, M.; Hutter, J. *Phys. Rev. B* **1996**, *54*, 1703–1710.

[13] Perdew, J. P.; Burke, K.; Ernzerhof, M. *Physical review letters* **1996**, *77*, 3865.

[14] Grimme, S. *Journal of Computational Chemistry* **2006**, *27*, 1787–1799.

[15] Boys, S. F.; Bernardi, F. d. *Molecular Physics* **1970**, *19*, 553–566.

[16] Hohenberg, P.; Kohn, W. *Phys. Rev.* **1964**, *136*, B864–B871.

[17] Kohn, W.; Sham, L. J. *Phys. Rev.* **1965**, *140*, A1133–A1138.

[18] Humphrey, W.; Dalke, A.; Schulten, K. *Journal of Molecular Graphics* **1996**, *14*, 33–38.

[19] Dennington, R.; Keith, T.; Millam, J. *GaussView Version 5*, Semichem Inc. Shawnee Mission KS 2009.

[20] Bruno, I. J.; Cole, J. C.; Edgington, P. R.; Kessler, M.; Macrae, C. F.; McCabe, P.; Pearson, J.; Taylor, R. *Acta Crystallographica Section B: Structural Science* **2002**, *58*, 389–397.